REPORT DOCUMENTATION PAGE

Form Approved OMB NO. 0704-0188

1. REPORT DATE (DD-MM-YYYY)	2. REPORT TYPE	3. DATES COVERED (From - To)
01-09-2015	Ph.D. Dissertation	-

4. TITLE AND SUBTITLE
Graphene-based Nanostructures and DNA-based Biomolecule Sensors

5a. CONTRACT NUMBER
W911NF-11-1-0024

5b. GRANT NUMBER

5c. PROGRAM ELEMENT NUMBER
611103

6. AUTHORS
Ke Xu

5d. PROJECT NUMBER

5e. TASK NUMBER

5f. WORK UNIT NUMBER

7. PERFORMING ORGANIZATION NAMES AND ADDRESSES
University of California - Irvine
Sponsored Project Administration
5171 California Avenue Suite 150
Irvine, CA 92697 -7600

8. PERFORMING ORGANIZATION REPORT NUMBER

9. SPONSORING/MONITORING AGENCY NAME(S) AND ADDRESS (ES)
U.S. Army Research Office
P.O. Box 12211
Research Triangle Park, NC 27709-2211

10. SPONSOR/MONITOR'S ACRONYM(S)
ARO

11. SPONSOR/MONITOR'S REPORT NUMBER(S)
58162-EL-MUR.110

12. DISTRIBUTION AVAILIBILITY STATEMENT
Approved for public release; distribution is unlimited.

13. SUPPLEMENTARY NOTES
The views, opinions and/or findings contained in this report are those of the author(s) and should not contrued as an official Department of the Army position, policy or decision, unless so designated by other documentation.

14. ABSTRACT
This research work contains three main parts. The ¯rst part is to investigate the electrical conductivity and dielectric properties of PMMA/Graphene Nanoplatelet composites with an emphasis on the percolation threshold. The second part is the study of a graphene-based FET structure including modelling the FET characteristics based on device theory calculation and simulation, and utilizing Raman Spectroscopy and Surface-Enhanced Raman Spectroscopy to verify active molecular components inside synthesized nanostructures. The third part is

15. SUBJECT TERMS
graphene-based nanostructures, DNA

16. SECURITY CLASSIFICATION OF:			17. LIMITATION OF ABSTRACT	15. NUMBER OF PAGES	19a. NAME OF RESPONSIBLE PERSON
a. REPORT	b. ABSTRACT	c. THIS PAGE			Peter Burke
UU	UU	UU	UU		19b. TELEPHONE NUMBER 949-824-9326

Report Title

Graphene-based Nanostructures and DNA-based Biomolecule Sensors

ABSTRACT

This research work contains three main parts. The ¯rst part is to investigate the electrical conductivity and dielectric properties of PMMA/Graphene Nanoplatelet composites with an emphasis on the percolation threshold. The second part is the study of a graphene-based FET structure including modelling the FET characteristics based on device theory calculation and simulation, and utilizing Raman Spectroscopy and Surface-Enhanced Raman Spectroscopy to verify active molecular components inside synthesized nanostructures. The third part is the sensor experiment part, which includes design, fabrication and testing of two biomolecular sensors using optical photolumescence measurements and graphene-based electrochemical measurements, respectively.

In the ¯rst part, we prepared poly(methyl methacrylate) (PMMA)/Graphite nanoplatelet (GNP) ensembles by in situ polymerization of MMA in the presence of GNPs with the aid of sonication and heating. Electrical conductivity and dielectric properties of the ensembles were measured using the four-point probe resistivity measurement method and a network analyzer. The results showed that the electrical behavior of PMMA/GNP ensembles can be described well by percolation theory. The percolation threshold of PMMA/GNP at room temperature was only about 1 wt% ¯ller content, much lower than that of the ensembles ¯lled with conventional graphite particles.

In the second part, we ¯rst modelled a graphene-based FET-like aptamer sensor for the case of an aptamer that binds to a cocaine surrogate. A voltage shift caused by electron trapping on the graphene surface is expected from the proposed charge sheet capacitance model and con¯rmed by experimental results. We then conducted Raman Spectroscopy and Surface-Enhanced Raman Spectroscopy measurements on the device surface, identi¯ed the signature spectrum of Methylene Blue (MB), and veri¯ed the successful functionalization of the DNA aptamer (terminated with MB) to the graphene surface.

In the sensor experiment part, we designed and fabricated a nanosensor comprised of thrombin binding aptamer (TBA) with 700NC InGaP QD on the 5' terminus and an Au nanoparticle quencher on the 3' terminus. Both potassium and lead ions bind to TBA, resulting in a conformational change that brings the Au quencher closer to the QD. Based on this mechanism we conducted Photolumescence measurements to detect potassium and lead ions. We also designed and fabricated a graphene-based FET structure to electrochemically detect these two ions. The sensor consists of a graphene-covered Si/SiO2 wafer with TBA attached to the graphene layer and terminated by a methylene blue molecule. Based on the same mechanism, when K+ and Pb2+ bind to TBA and cause a conformational change, MB will move closer to the graphene surface and donate an electron. The abundance of K+ and Pb2+ can be determined by monitoring the current across the source and drain channel. Experimental results con¯rmed that drain current decreased as ion concentration increased.

Graphene-based Nanostructures and DNA-based Biomolecule Sensors

BY

KE XU
B.E., Zhejiang University, Zhejiang, China, 2009
M.S., University of Illinois at Chicago, Chicago, IL, 2013

THESIS

Submitted as partial fulfillment of the requirements
for the degree of Doctor of Philosophy in Electrical and Computer Engineering
in the Graduate College of the
University of Illinois at Chicago, 2014

Chicago, Illinois

Defense Committee:

Michael A. Stroscio, Chair and Advisor
Mitra Dutta
Zheng Yang
Junxia Shi
Alan Nicholls

This thesis is dedicated to my family, especially my parents Mrs. Yihe Pan and Mr. Dai Xu, whose great love and everlasting support accompanies me from my childhood to now and beyond.

ACKNOWLEDGMENTS

I would like to thank my advisor, Dr. Michael A. Stroscio for his consistent guidance, unfailing support and enduring patience throughout my graduate study. His wisdom, vision and encouragement helped me accomplish various research projects and will benefit me more in my future life.

I would also like to extend my sincere acknowledgements to all the people who have contributed in every little way to the successful completion of my research work at UIC. I would like to thank Dr. Mitra Dutta for sharing her knowledge and time; Dr. Zheng Yang, for providing valuable advices and information on microfabrication techniques; Dr. Kebin Low, for his help and guidance in Raman Spectroscopy and TEM measurements; Dr. Siddhartha Ghosh, for contributing his expertise on the sensor test procedure. I would also like to extend my gratitude to my dissertation committee members Dr. Lucy Shi and Dr. Alan Nicholls for valuable discussions and suggestions on shaping my thesis.

Many thanks go to all members of the Nanoengineering research group especially Xenia Meshik, Kimber Brenneman, Shripriya Poduri, Donna TsaiChin Wu, Jun Qian, Mohsen Purahmad, Sidra Farid, Nanzhu Zhang, Min Choi and Elaine Yi Lan for their help and friendship. Special thanks go to Xenia, without her great collaboration and help this effort would not have been possible.

I will forever be thankful to my former high school teacher Lisa. She is the most inspirational teacher and one of the kindest people I know. I still think fondly of my time as a student in

her class. She passed away while I was pursuing my PhD in the United States, but her memory will be with me always.

Finally, I would like to give my deepest appreciation to my family, for their love and support at all times.

KX

TABLE OF CONTENTS

TABLE OF CONTENTS (Continued)

CHAPTER **PAGE**

TABLE OF CONTENTS (Continued)

LIST OF TABLES

LIST OF FIGURES

LIST OF FIGURES (Continued)

FIGURE **PAGE**

LIST OF ABBREVIATIONS

AFM	Atomic Force Microscope
CMOS	Complementary Metal Oxide Semiconductor
CNT	Carbon Nanotube
MWNT	Multi-walled Nanotube
SWNT	Single-walled Nanotube
DNA	Deoxyribonucleic Acid
dsDNA	Double-stranded DNA
FET	Field Effect Transistor
GFET	Graphene-based Field Effect Transistor
GNP	Graphene Nanoplatelet
GNR	Graphene Nanoribbon
CVD	Chemical Vapor Deposition
LPCVD	Low-pressure Chemical Vapor Deposition
QD	Quantum Dot
SEM	Scanning Electron Microscope
STM	Scanning Tunneling Microscope
TEM	Transmission Electron Microscope

LIST OF ABBREVIATIONS (Continued)

PMMA	Polymethyl Methacrylate
MB	Methylene Blue
TE	Tris Ethylene diamine tetra acetic acid
MWCO	Molecular Weight Cut-off
PBS	Phosphate Buffered Saline
TBA	Thrombin Binding Aptamer
DPV	Differential Pulse Voltammetry

SUMMARY

This research work contains three main parts. The first part is to investigate the electrical conductivity and dielectric properties of PMMA/Graphene Nanoplatelet composites with an emphasis on the percolation threshold. The second part is the study of a graphene-based FET structure including modelling the FET characteristics based on device theory calculation and simulation, and utilizing Raman Spectroscopy and Surface-Enhanced Raman Spectroscopy to verify active molecular components inside synthesized nanostructures. The third part is the sensor experiment part, which includes design, fabrication and testing of two biomolecular sensors using optical photolumescence measurements and graphene-based electrochemical measurements, respectively.

In the first part, we prepared poly(methyl methacrylate) (PMMA)/Graphite nanoplatelet (GNP) ensembles by in situ polymerization of MMA in the presence of GNPs with the aid of sonication and heating. Electrical conductivity and dielectric properties of the ensembles were measured using the four-point probe resistivity measurement method and a network analyzer. The results showed that the electrical behavior of PMMA/GNP ensembles can be described well by percolation theory. The percolation threshold of PMMA/GNP at room temperature was only about 1 wt% filler content, much lower than that of the ensembles filled with conventional graphite particles.

In the second part, we first modelled a graphene-based FET-like aptamer sensor for the case of an aptamer that binds to a cocaine surrogate. A voltage shift caused by electron trapping

on the graphene surface is expected from the proposed charge sheet capacitance model and confirmed by experimental results. We then conducted Raman Spectroscopy and Surface-Enhanced Raman Spectroscopy measurements on the device surface, identified the signature spectrum of Methylene Blue (MB), and verified the successful functionalization of the DNA aptamer (terminated with MB) to the graphene surface.

In the sensor experiment part, we designed and fabricated a nanosensor comprised of thrombin binding aptamer (TBA) with 700NC InGaP QD on the 5' terminus and an Au nanoparticle quencher on the 3' terminus. Both potassium and lead ions bind to TBA, resulting in a conformational change that brings the Au quencher closer to the QD. Based on this mechanism we conducted Photolumescence measurements to detect potassium and lead ions. We also designed and fabricated a graphene-based FET structure to electrochemically detect these two ions. The sensor consists of a graphene-covered Si/SiO_2 wafer with TBA attached to the graphene layer and terminated by a methylene blue molecule. Based on the same mechanism, when K^+ and Pb^{2+} bind to TBA and cause a conformational change, MB will move closer to the graphene surface and donate an electron. The abundance of K^+ and Pb^{2+} can be determined by monitoring the current across the source and drain channel. Experimental results confirmed that drain current decreased as ion concentration increased.

CHAPTER 1

INTRODUCTION

1.1 Background and Motivation

For the past forty years, the semiconductor industry has been growing exponentially based on Moore's law (1) which described the development path of Si-based semiconductor industry. Moore's law states that the number of transistors in integrated circuits doubles every two years (2). The entire electronics industry has been pushing the boundaries of innovation in order to make devices with higher speed, smaller size and increased complexity while at the same time maintaining low power consumption and low cost. However, when the device scale approaches tens of nanometers, Moore's law reaches the physical limitation and thermal management issue. In 2012, Intel employs the newest 22 nm process technology in its latest i3, i5 and i7 CPU series called "Ivy-Bridge", it already starts to encounter the difficulties and slowdown in speed of making faster processors. The scaling limitations motivate the research on new nanomaterials and technologies that have the potential to replace or enhance current silicon systems.

After the first appearance of CNT in 1990 (3) carbon has emerged as a front-runner underlying carbon-based nanotechnology. Carbon has various crystalline allotropes such as diamond, graphite, graphene, nanotubes and Buckminsterfullerenes. Since the discovery of the technique to produce graphene flakes called mechanical exfoliation in 2004 (4; 5), graphene has been claimed as the saviour of Moore's law. The consensus in the scientific community is that tran-

sistor linewidth cannot be reduced for much longer without increasing fabrication costs to such a level that the cost of transistors would be too high. 2010 has been claimed as the year of graphene, not only because the Nobel Prize in Physics in 2010 were awarded to Andre Geim and Konstantin Novoselov for their discovery of graphene, but also due to the fact that around 3000 graphene related articles were published and roughly 400 patent applications filed. Graphene research has been mostly focused on transistors and thin film applications, but the interest in different applications of graphene is growing rapidly (6). Of all of the suggested applications of graphene, the use of graphene to make graphene-based field effect transistor seems the one most closest to emerge.

1.2 Polymer/Graphite nanoplatelet composites

Polymer ensembles based on disperse conducting fillers, such as natural graphite flakes and metal powders, embedded in insulator matrices have been sought in an effort to prepare electrically conducting ensembles that are of great interest to scientists and researchers in the past few decades. Their unique electrical and mechanical properties combined with the light weight, flexibility, and transparency of polymers has resulted in efforts underlying a wide range of practical applications in electromagnetic shielding, light-emitting diodes, batteries, etc. (7; 8; 9). Research efforts on polymer nanoensembles in the past decades have resulted in advancements in improving mechanical properties, thermal stability, electrical and thermal conductivities, dielectric performances and other attributes (10; 11; 12). Among the variety of conducting fillers, natural graphite flakes have been widely studied. They are abundant in

natural sources and possesses excellent electrical conductivity in the range of about 10^4 S/cm at room temperature (13).

Complex ensembles of nanostructures have been studied in a variety of media including aqueous media (14); moreover, thin graphite-based structures (15) and graphene-based nanosturctures have been analyzed in terms of their novel heat transport and confined phonon properties, respectively. In this work, ensembles of nanometer-thickness graphite structures are considered in PMMA medium.

Graphite nanoplatelets (GNPs), also known as expanded or exfoliated graphite (EG), serve as a 2D graphite nanofiller having stacked graphene layers. The graphene layers are stacked and bonded by weak van der Waals forces with a constant interval distance between layers (16). The thicknesses of GNPs are usually in the range of nanometers while their diameters may be in the micrometer scale, which results in high specific surface area and the high aspect ratios of GNPs. Compared with other classic 2D nanofillers, such as clay platelets or rubber, GNPs have lower mass density and higher electrical and thermal conductivity. Polymer/GNP ensembles have been the subjects of research ever since the fabrication of monolayer graphene with extraordinary electronic and mechanical properties in 2004 (17; 18).

1.3 Graphene and graphene-based field effect transistor

Graphene is a two-dimensional network of single layer sp^2-bonded carbon atoms arranged on a honeycomb lattice. The name graphene is sometimes misleadingly used to describe multiple layers. Multilayer graphene can have up to ten layers and still be called graphene. It should be noted that the variation in properties of graphene is quite significant when going from one layer

to several. Ten layers is the limit where graphene becomes graphite, which is stack of graphene sheets bound by weak van der Waals forces.

Graphene has exceptional electrical, optical, mechanical and thermal properties due to its atomic structure and special band structure (19). Graphene is a zero-bandgap semiconductor. In other words, it can be considered both as a semiconductor and as a semi-metal. Wallace (20) first studied the band structure of graphene in theory and revealed its unusual semi-metallic behavior. While the zero-bandgap in intrinsic graphene makes graphene uniquely interesting, the lack of a bandgap can be a major engineering issue. Due to its zero-bandgap, graphene is particularly difficult to be switched off from a conductive state to a non-conductive state, and thus difficult to be used as a solid state switch. Bilayer graphene or graphene nanoribbon (GNR) can avoid this problem because both of them can have a band gap under the right condition. It is to be noted that the zero-bandgap of large area graphene is not an issue in radio frequency (RF) applications.

Among Graphene's electrical properties, high electron mobility (21; 22) and ballistic transport of charge carriers (23) are of the most interest to researchers. Similar as in carbon nanotube (CNT), the pseudo spin nature of the charge carries in graphene can cause the absence of backscattering and resulting in the high mobility (21; 22). In the meantime, weak electron-phonon coupling, the near defect-free lattice, and high sound velocity can also contribute to the high current density and current sustainability of graphene. Graphene can sustain current density up to 510^8 A/cm^2, which is about 1 μA per atomic row of carbon atoms (24). The high mobility and the quantization of conductance in narrow channels can contribute to

ballistic transport of charge carriers in the sub-micron range (23; 25). Graphene technology is especially promising because it can be easily integrated into the existing planar processing infrastructure, grown on various substrates including silicon dioxide which can processed by conventional semiconductor methods. Thanks to graphene's exceptional electronic properties, ultrafast electronic devices operating in the frequencies range of up to THz are expected.

Graphene has practical applications in various fields including graphene thin film electrodes, graphene-based nanocomposites and graphene-based field-effect transistor (GFET). The structure of a Graphene-based FET is identical to a silicon FET. A typical field-effect transistor is an electronic device with three terminals. A terminal known as gate can create an electric field to control the conductivity between the other two of the terminals known as source and drain. The free carrier density in the channel between source and drain can be tuned by gate voltage, leading to a current change controlled directly by gate voltage. This shift of current functions as a switch which indicates an "On" state when the current value is in high and an "Off" state when current in the channel is very low. The operation principle of a graphene-based field effect transistor is based on the ambipolar electric field effect in single and few-layer graphene (4). The ambipolar field effect is due to a small overlap in the valence and conductance bands. Graphene-based FET, Carbon Nanotube (CNT)-based FET and Nanowire-based FET are being considered by the semiconductor industry as a possible alternative to replace the conventional silicon field-effect transistor (26; 27). In the case of carbon nanotubes, all constituent atoms are at the surface and any small change on the surface can lead to a large change in electrical current, which made possible of developing sensors with exceptional sensitivity. While

offering similar electronic properties as CNTs, the fact that graphene has planar geometry and its ability to be processed with current complementary metal oxide semiconductor (CMOS) technology gives graphene a significant advantage over CNTs.

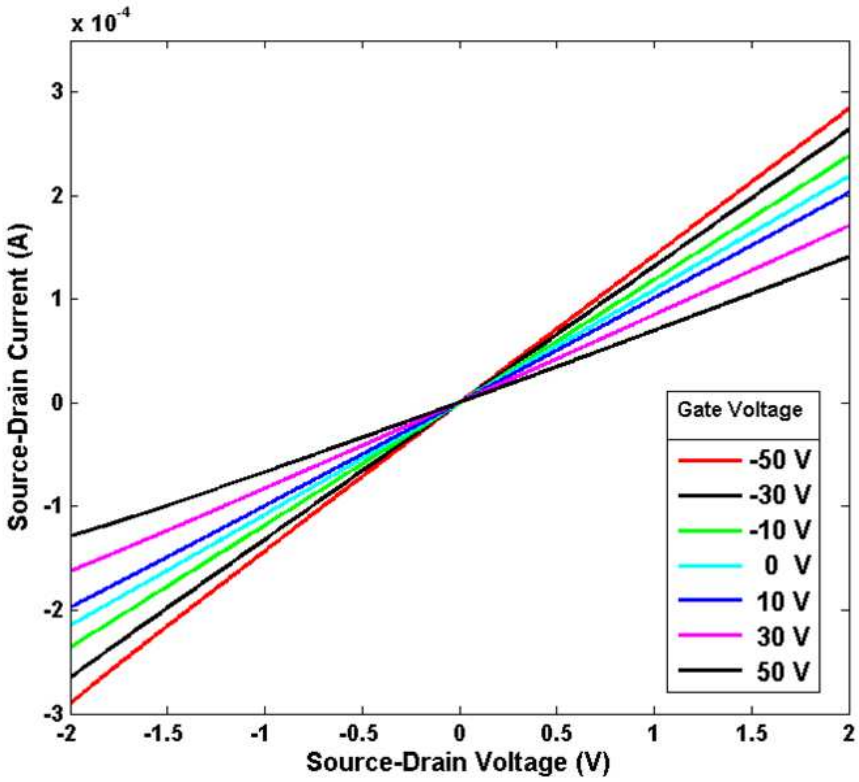

Figure 1. Voltage-current characteristic of a graphene-based FET structure.

Figure 1 shows a typical source-drain current (I_{ds})/source-drain voltage (V_{ds}) characteristics of graphene-based FET sensors. Single layer and bilayer graphene were used as sensing substrate. Graphene were grown in collaboration with Army Research Laboratory using low pressure chemical vapor deposition (LPCVD) on copper foil and transferred onto Si/SiO_2 substrate. The Si/SiO_2 substrate consists of 525 μm of n^{++} Si wafer coated with 296 nm of SiO_2. The thickness of graphene layers was later confirmed with Raman spectroscopy to be consisting of 6% single layer and 94% bilayer graphene. The FET structure was fabricated on top of graphene surface with 5 nm thick chromium and 45nm thick gold as source and drain electrodes. Channel length and width were both set at 2 mm for easy application in future measurement. Voltage was applied on degenerately doped silicon which was used as the gate terminal. Conductivity between source and drain can be effectively modulated by gate voltage. When the gate voltage varied from -50 V to 50 V, the conductance of the device decreased, indicating a p-type semiconductor behavior under ambient conditions.

1.4 Graphene- and aptamer-based biosensors

1.4.1 Aptamer and aptamer-based biosensors

Aptamers are short strands of featured oligonucleic acid sequences typically 90-200nm long containing about 30-80 oligonucleotides. Aptamers can recognize specific ligands or molecules in analytes and bind to those target molecules. Aptamers can detect a wide range of molecules including ions, nucleic acids, small molecules, proteins, and even tissues, cells, and organisms. Within a short period of time in 1990, three separate groups independently developed in vitro selection and amplification technique for the isolation of specific nucleic acid sequences able to

bind to target molecules with high affinity and selectivity (28; 29; 30). Both RNA and DNA aptamers are found by a process called SELEX (Selection Evolution of Ligands by Exponential Enrichment). During the process, aptamers are selected and isolated from vast populations of random sequences, and engineered through repeated rounds of in vitro selection to be able to bind to specific molecular targets. Aptamers are sometimes called synthetic antibodies because they have similar properties in a number of applications.

Biosensors are integrated devices capable of detecting the existence of target molecules or ligands by using a particular recognition element and then providing semi-quantitative or quantitative analytical information. Biosensors detect the presence of target by monitoring the optical, electronical or mass changes generated from the interaction between the recognition component and the target analyte. When aptamers are used as the recognition element it is also called an aptasensor (31). Aptamer-based biosensors can takes advantage of the high selectivity and tunable properties of aptamers. Comparing with antibodies, aptamers have a wide range of advantages such as smaller size, chemically stable, able to bind to drugs and toxic substance, ability to be labeled without affecting affinity, low cost compared with antibodies, etc.

Based on different sensing mechanism, two types of biosensors are most widely used known as optical biosensor and electrochemical biosensor. Optical biosensors utilize fluorescent detection technique to detect optical bioassays. Thanks to aptamers ability to be labeled without affecting affinity, fluorescent dyes, different fluorophores and quenchers can be easily functionalized on the end of aptamers. Fluorescent detection also has the advantage of inherent capability for real-time detection. One of the first examples of an optical aptamer-based sensor was reported

by Kleinjung et al. for the detection of L-adenosine. They manage to immobilize a biotinylated RNA aptamer on streptavidin-derivatized optical fibers (32). The approach evaluated the association and dissociation kinetic and showed the capability of aptamers for the sub-micron scale detection of specific analytes. Several other approaches have been developed for converting aptamers into fluorescent sensing probes. A frequently adopted method is using aptamer-based molecular beacons. A molecular beacon is a nucleic acids probe that will undergo spontaneous conformational change when encountering specific target or complementary nucleic acids and translate the conformational change into a variation in fluorescent properties. An aptamer-based molecular beacon is a modified version of traditional molecular beacon and usually called aptabeacon (33). It places an aptamer sequence in a hairpin structure, and functionalizes the two ends with a fluorophore and a quencher, respectively. Theoretically, any known aptamer can be converted into a molecular aptamer beacon by adding a small sequence of nucleotides to its 3'-end as well as to its 5'-end (33). For example, a quencher can be covalently attached to the 3'-end, and a fluorophore can then be added to the 5'-end. When the target ligand is absent, the beacon will form into a stem structure placing the fluorophore and quencher to be close to each other. In this state there will be no fluorescence signal because light energy is transferred to the quencher and the fluorophore is quenched. In the presence of ligand, the aptamer will bind to the target ligand and forming a probe. The binding of target is more stable and stronger than the stem structure and thus it can disrupt the stem, open the aptamer, separate quencher from the fluorophore and resulting in fluorescence signals that is able to be measured quantitively or semi-quantitively (34).

Different from optical biosensors, electrochemical biosensors monitor the electrical signal generated during the interacting between the aptamers and target analytes. Typically the amplitude of the electrical signal is proportional to the analyte concentration. Based on the assay format and the method of detection, the electrochemical aptamer-based biosensors can be divided into three major types. The first type is called sandwich and competition-type, which involves the use of an electrode-bound aptamer to bring a complex composed of the target and some redox-active targets to the electrode. In the second type electrochemical impedance spectroscopy is used to detect targets adsorbed onto an aptamer-terminated electrode surface. And the third type uses electrochemistry to monitor binding-related conformational changes in an electrode-bound aptamer.

Xiao et al. (35) reported detection in a typical beacon format based on a 3-D conformational change with thrombin binding aptamer. The aptamer undergoes a structural rearrangement that allows thrombin detection using a beacon without a stem-loop. Thrombin is a proteolytic enzyme which facilitates blood clotting by converting fibrinogen into fibrin, which can also be used as a tumor marker in the diagnosis of pulmonary metastasis. The aptamer molecular beacon was constructed by binding a methylene blue molecule to one end of the aptamer and a thiol group to the other end. The thiol group functions as a linker that can be attached on gold electrode surfaces. Before interaction with thrombin, the aptamer was elastic and able to interact with the electrode surface and transferring electrons. However, after interaction occurred, conformational change creates a longer electron-tunneling distance and thus decreasing the signal. Similar aptamer molecular beacon approach was used by the team for the electro-

chemical detection of platelet-derived growth factor in picomolar range, and demonstrated this aptamer-based biosensor directly in blood serum (36).

Compared with the "signal-off" structure in which the electrical signal decrease as a result of binding, an improved "signal-on" architecture was later discovered by Radi et al. (37) in which the binding of the target analyte resulted in an increase in the signal. In this case, the aptamer molecular beacon had a ferrocene label with shorter spacers on both end. Detection was conducted using cyclic voltammetry, DPV and impedance measurements. Before thrombin is introduced to the structure, the ferrocene label is far from the electrode surface and could not provide any electron transfer to the surface. When thrombin is present, the aptamer would form a G-quadruplex and ferrocene label would bend close to the electrode allowing effective electron transfer as well as signal generation. With the use of DPV a detection limit of 0.5 nM can be achieved with a linear range of 5-35 nM. Xiao et al. (38) made similar efforts to modify their previous structure and fabricate "signal-on" electrochemical aptamer sensor. They started with double-stranded DNA consisted of a short DNA sequence tagged with methylene blue (MB) that can hybridize with an aptamer, and a sequence complementary to it which contained the anti-thrombin aptamer sequence. The duplex of DNA maintained the redox label at "standing" position with a long enough distance from the electrode surface. When thrombin is added to the complex, the complementary sequence would displace and the single stranded DNA with methylene blue tagged in one end would approaches near the electrode surface and producing electric current.

1.4.2 Aptamer-based biosensors using graphene-based FET structure

The merit of using aptamers in graphene-based biosensor with FET structure lies in their small size. One critical definition here is called Debye length which is the typical distance required for screening the surplus charges contributed by the mobile electric carriers present in a nanostructure. Antibodies are widely used as sensing elements. However, the size of antibodies is about 10 nm, which is much larger than the Debye length or electrical double layer that is about 3 nm in 10 mM ionic concentration. As a result, the recognition of target binding process might occur outside the electrical Debye length and lead to very weak potential changes observed on the electrical contacts. Aptamers, on the other hand, have an average of 2 nm for 30 bases, which is within the Debye length and can enable the perturbation of gate potential by target analytes that interact with the aptamers.

Before graphene-based FET structure is integrated into biomolecule sensors, carbon nanotube-based FET structure has been massively researched in developing chemical and biological sensors. So et al. fabricated a single-walled carbon nanotube (SWNT) field-effect transistor to monitor the binding processes between aptamer and thrombin (39). It is known that SWNTs behave as p-type semiconductors in ambient atmosphere. SWNTs were immobilized between source and drain electrodes, and anti-thrombin aptamers were attached on the SWNTs. The reaction between aptamer and thrombin altered conductance between source and drain, thus enabling electrical detection of thrombin.

However, the applications of CNTs are often plagued with several problems. For example, it is difficult to separate semiconducting nanotubes from metallic nanotubes. Also, when only

a few CNTs are used, it is in many cases challenging to manipulate them for device fabrication because they are too small compared with large-sized biomolecules. On the other hand, Graphene, with similar properties as CNT but comes in a flat structure, is an ideal substrate for fabricating biosensors.

Xu et al. reported a graphene-based and aptamer-based biosensor with cocaine as detecting target (37). One end of the aptamer is attached with methylene-blue (MB) which functions as an electron donor. 1-pyrenebutanoic acid, succinimidyl ester (merchandise name: P130) as the red dot in the figure is used as linker molecule which contains the pyrene group that can noncovalently bind to the graphene surface. Due to the overlapping of -bonds between aromatic side chains, the highly aromatic pyrene group could interact strongly with the basal plane of graphene via -stacking. Thanks to the small size of cocaine aptamer which is about 2-nm in length with 30 bases, the whole structure is within the Debye length. When the target cocaine molecule is present, the aptamer will undergo a conformation change and lead to a closer distance between the MB and the graphene surface. When the MB bends within the proximity of graphene surface, it can provide electrons and cause a current shift in the I-V characteristics of the graphene-FET.These results from current graphene-based and aptamer-based biosensors show exceptional electronic response and the ability to support cell adhesion and growth, which proves the promising potentials of graphene in making nanoscale biomolecule sensers as well as applications in detecting dynamic bimolecular analytes.

CHAPTER 2

ELECTRICAL CONDUCTIVITY AND DIELECTRIC PROPERTIES OF PMMA/GRAPHITE NANOPLATELET ENSEMBLES

2.1 Introduction

Poly(methyl methacrylate) (PMMA)/Graphite nanoplatelet (GNP) ensembles were prepared by in situ polymerization of MMA in the presence of GNPs with the aid of sonication and heating. The polymers were locked into the pores of the exfoliated/expanded graphite nanosheets and remained in them after polymerization took place. The objective of our work is to investigate the electrical conductivity and dielectric properties of PMMA/GNP ensembles with an emphasis on the percolation threshold. The graphite flakes from XG Sciences, Inc. are used as a means of providing a comparison with previous studies. Electrical conductivity and dielectric properties of the ensembles were measured using the four-point probe resistivity measurement method and a network analyzer. The results showed that the electrical behavior of PMMA/GNP ensembles can be described well by percolation theory. The electrical conductivity of the ensemble was found to exhibit an insulator-conductor transition at a very low percolation threshold for GNPs. The percolation threshold of PMMA/GNP at room temperature was only about 1 wt% filler content, much lower than that of the ensembles filled with conventional graphite particles. Results showed that the difference in filler geometry (high as-

pect ratio and surface area) has a very significant effect on forming a conducting network in the PMMA matrix and improves both electrical and dielectric properties.

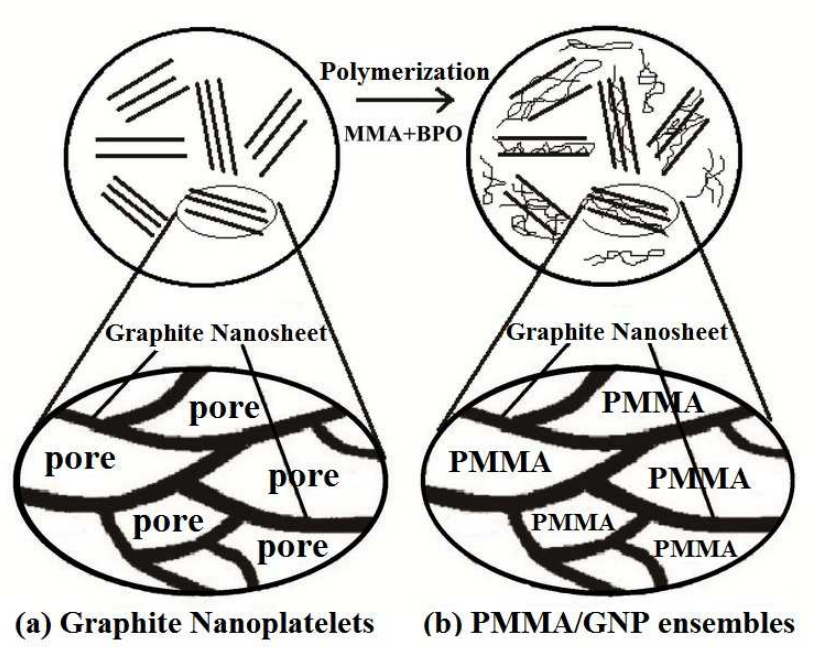

Figure 2. Illustrative model for morphology development during *in situ* polymerization of the PMMA/GNP ensemble.

2.2 Experimental Procedure

2.2.1 Material

PMMA was prepared by the *in situ* polymerization using the methyl methacrylate (MMA) monomer (Sigma-Aldrich, USA). Graphite Nanoplatelets with an average thicknesses of approximately 15 nanometers and diameters of 25 microns were supplied by XG Science, Inc. and used for the source of conducting filler. The conductivity of the Graphite Nanoplatelets(GNP) is 10^7 S/m with a surface area of 50-80 m^2/g. Benzoyl peroxide (BPO) was obtained from Sigma-Aldrich as the free radical initiator and was used as received.

2.2.2 In situ polymerization and Preparation of PMMA/GNP ensembles

Initially, MMA monomer was mixed with various ratios of GNPs in a tightly sealed test tube. To achieve a more uniform dispersion of GNPs in the MMA liquid, the test tube was put into high power sonication in the ultrasonic bath for 20 minutes at a temperature of 55 °C. Sonication was continued and was followed by adding the initiator BPO (0.5 wt% of monomer). The whole mixture was kept heated and sonicated for another 3 hours. Continuous sonication provides better dispersion of GNPs in the subsequent polymerization process. The test tube was transferred to a heated oil bath at 60 °C for 10 hours for the polymerization process to take place. Constant heating is required for a uniform polymerization rate. After 10 hours, the suspension became sticky and turned into a black solid. Circular samples with diameters of about 2.5 cm and thicknesses of around 0.8 cm were cut down from the black solid for measurement.

2.2.3 Characterization and Measurement

2.2.3.1 Conductivity Measurement

Both surfaces of the sample were polished with sandpaper to remove the undesirable polymer surface layer and to eliminate surface unevenness. The electrical conductivity of PMMA/graphite ensembles was measured at room temperature by four probe techniques using a HP 34401A digital multimeter. The sample was cut into slim specimens with diameters of 2.5 cm and thicknesses of 0.4 cm for testing. Conductive brass wires were hot pressed to the surface as electrode for good contact. For the pure PMMA matrix and for the ensembles with low filler content (where the conductivities of samples were lower than the detectable range of the four-probe resistivity test system), the resistivities were determined by a FLUKE45 digital model resistivity meter.

2.2.3.2 Dielectric Measurement

Dielectric measurements were conducted using a HP/Agilent 8753ES Network Analyzer. In order to have better contact with the sample, an 8060 MicroManipulator Probing System was used to connect the Network Analyzer with the sample surface. After polishing, silver paint was brushed on both planar surfaces of the sample to be used as an electrode and provide good conductivity. The measurement was carried out in Parallel Plate mode under room temperature conditions. The impedance of the sample as well as the S_{11} reflection coefficient were measured in the frequency range of 5 KHz–1 MHz. Calibration was done with a 2.4 mm calibration kit. Several resistances and capacitances with known values were tested before measurement to make sure the calibration is accurate.

2.3 Result and Discussion

Electrical Conductivity of PMMA/GNP ensembles

Figure 3 shows the variations of the electrical conductivity (σ) of PMMA/GNP with respect to filler content between 0% (PMMA only) and 5% GNP. In the initial stage the conductivity of the materials is in the magnitude of 10^{-16} S/cm when no GNP had been added. This is consistent with the magnitude typical of an insulator. A feature of interest in this figure is that there is an abrupt conductivity transition that occurs at a critical filler content of about 1.2 wt%, which can be designated as the percolation threshold. After arriving at this critical value the conductivity levels remain almost stable with little increase with the filler content. The ensembles' conductivities are about 10^{-5} S/cm at 3 wt% and 10^{-4} S/cm at 5 wt%, which is nearly consistent with the magnitude of a semiconductor. According to the percolation theory, the percolation threshold (ϕ) corresponds to the onset of the transition from an insulator to a semiconductor. The electrical conductivity of PMMA/GNP ensembles exhibited a significant transition with regard to the increase of filler content. This transition could also be explained by the formation of a conductive network in the nanoensembles.

The advantage of graphite nanoplatelets over conventional graphite flakes as conductive fillers is conspicuous, including low electrical percolation threshold and high level-off electrical conductivity after percolation. On the one hand, the low electrical percolation threshold can be ascribed to the filler shape and the surface area per gram of filler. For example, though the natural graphite flakes also contain layering structure the same as the GNPs, the surface area of each particle is much smaller than the GNPs, which results in much lower aspect ratio. So

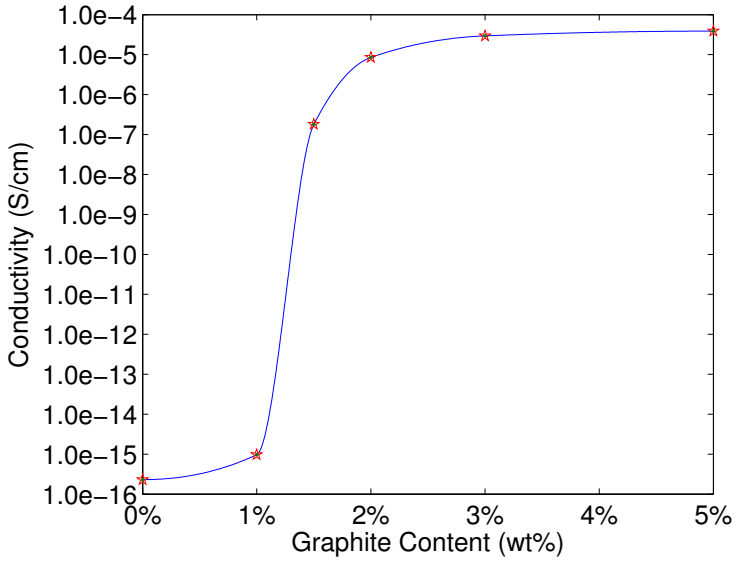

Figure 3. Electrical conductivity of PMMA/GNP as a function of weight fraction.

for polymer/GNP ensembles, higher aspect ratio and surface area of fillers will lead to a lower percolation threshold because the fillers with high aspect ratio can rapidly form conductive networks throughout the ensembles (40).

On the other hand, the PMMA/GNP ensembles synthesized by "wet" methods, such as in situ polymerization with the assistance of ultrasonication, usually have a lower percolation threshold (41). This could be attributed to two major factors: dispersion quality and level of exfoliation in GNPs. In the *in situ* polymerization technique, the monomers and polymer molecular chains can get into the porous GNPs, and with the help of ultrasonication treatment not only can the dispersion quality be improved, but also the number of exfoliated GNPs will

increase and result in higher exfoliation degree. Accordingly, the conductive network can be formed at a lower level. One thing to point out is that sufficient adsorption of the PMMA molecular chains into pores of the GNPs was also affected by solution concentration. If the concentration is too high, the higher viscosity may impede the polymer chains from entering the smaller pores of the graphite and thus lead to poor dispersion of GNPs in the polymer.

Power Law Model

It had been well known that a power law model is applicable to explain the critical relationship between the conductivity of ensemble and concentrations of conducting filler around the percolation threshold (42; 43); herein, the conductivity is modeled using the following equations:

$$\sigma = \sigma_0(\phi - \phi_c)^t,$$

$$\log \sigma = \log \sigma_0 + t \log(\phi - \phi_c).$$

In these equations, σ is the conductivity of the ensemble, σ_0 is the conductivity of the conducting filler, ϕ is the volume fraction of conducting filler, ϕ_c is the percolation threshold concentration of filler and t is a critical exponent indicating the power of the electrical conductivity increase. In order for these equations to be valid, all the calculations must be conducted above but not far from the percolation threshold. The universal value for critical exponent in a three dimensional lattice is between 1.5 and 2.0 (44; 45).

As shown in Figure 4, the log (σ) vs. log (ϕ-ϕ_c) plot is obtained by converting the mass fraction of the GNPs in the polymers to volume fraction of the GNPs in the polymers, using the densities of the polymer monomers and GNPs. From the best linear fit of the experimental data presented in the previous section and the log-log plot of the power laws, both t and σ_0 may be estimated from the slope and intercept of the line, respectively. The value of t is found to be 2.41 which is higher than the value predicted by the power law model. However, similar high value is reported by many other researchers such as Srivastava *et al.* (46) with polystyrene as nanofiller and Liu *et al.*(47) with carbon nanotubes.

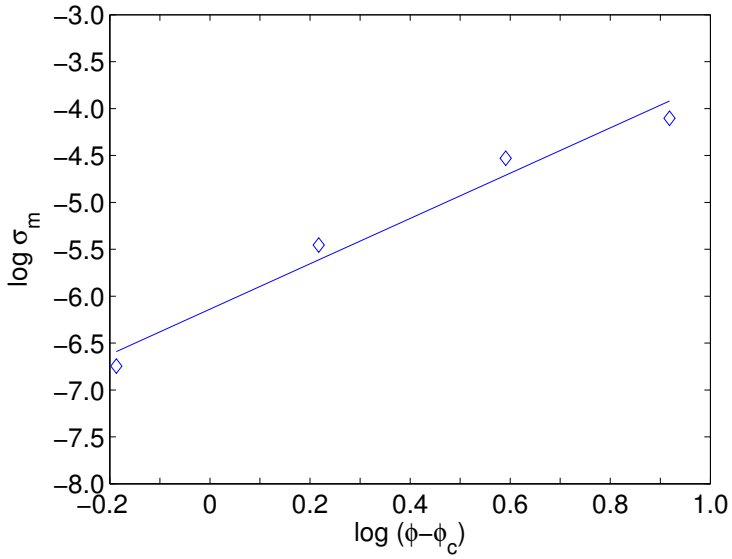

Figure 4. Log(σ) versus log(ϕ-ϕ_c) and best linear fit of experimental data.

This higher than universal value of critical exponent may be due to the non-universal transport behavior of the PMMA/GNP ensembles. It had been found that high values of t usually occur in extreme geometries of conductive particles, with the accompany of tunneling conduction that result in non-universal exponent (42). In this study, the high aspect ratio of GNPs provides a relatively extreme geometry in the first place. Also it is entirely possible that the acid groups on the GNP surface, which contains oxygen within themselves, could cause GNPs to be coated by PMMA films. Consequently, non-universal transport will occur as a result of tunneling conduction through the insulating PMMA barrier.

Dielectric Properties of PMMA/GNP ensembles

The complex dielectric constant is a function of the frequency (f) and is defined by

$$\varepsilon(\omega) = \varepsilon'(\omega) - j\varepsilon''(\omega) = |\varepsilon|e^{-j\delta}, \tag{2.1}$$

where $\omega = 2\pi f$ is the angular frequency of the measuring electric field. The real part $\varepsilon(\omega)$ is mostly known as the relative permittivity or dielectric constant and the imaginary part $\varepsilon''(\omega)$ generally referred as the loss factor. δ is the dielectric loss angle which is used in defining loss tangent or dissipation factor (DF). The dissipation factor $\tan\delta$ is expressed as the ratio of $\varepsilon''(\omega)$ to $\varepsilon'(\omega)$. It is a measure of loss-rate of energy of a mode of oscillation, either mechanical, electrical or electromechanical, in a dissipative system.

In dielectric analysis, the loss factor corresponds to the conductivity of the materials. In parallel plate electrodes mode which we used in our experiment, the loss factor (ε'') can be calculated as follows:

$$DF = \tan\delta = \frac{\varepsilon''(\omega)}{\varepsilon'(\omega)} = \frac{i^2 ESR}{i^2|X_c|} = \omega C \cdot ESR, \tag{2.2}$$

where C is the lossless capacitance and ESR is the Equivalent Series Resistance. Equivalent Series Resistance represents losses in a capacitor/inductor-containing system that may be caused by dielectric conduction electrons and dipole relaxation phenomena. Typically in a dielectric material, only one of the above two causes dominates the loss. For the case of the conduction electrons being the dominant loss, then

$$ESR = \frac{\sigma}{\varepsilon\omega^2 C}, \tag{2.3}$$

thus,

$$\varepsilon'' = \varepsilon \cdot \frac{\sigma}{\varepsilon\omega} = \frac{\sigma}{2\pi f}. \tag{2.4}$$

So the loss factor is related to the conductance (σ) and frequency.

Figure 5 shows the loss factor (ε'') versus graphite content when we convert the conductance value we obtained into loss factor using the formula above. Also if we do some simple simulation of the loss factor with respect to frequency change, the result can be shown on the same graph. Both the loss factor value and the decreasing trend with frequency are consistent with the results of some other research groups (48; 49), who use a dynamic mechanical analyzer to determine the loss factor change with filler content. In order to measure the dielectric

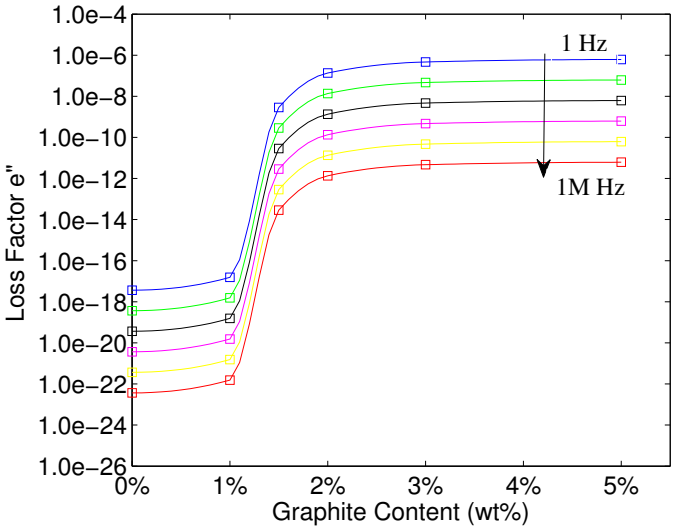

Figure 5. Loss factor ε'' of PMMA/GNP vs. graphite filler content with frequency from 1 Hz to 1M Hz.

constant and dissipation factor we have used a Network Analyzer. The network analyzer can

measure the scattering coefficient of the system. If measured in single port system, the scattering coefficient is the same as the value of reflection coefficient (Γ). The relationship between reflection coefficient of complex impedance of the measurement sample is

$$\Gamma^{(1)} = \frac{Z_{in}^{(1)} - Z_0}{Z_{in}^{(1)} + Z_0}. \tag{2.5}$$

With the characteristic impedance Z_0 known to be 50 ohms, complex impedance as well as the real and imaginary part of S_{11} of the sample measurement may be obtained by the network analyzer. The complex impedance remains stable in the range of 10^3–10^5 Hz, with the real part of impedance having a magnitude of about 10^5. This value agrees with our previous measurement of conductivity and a similar result had been reported by others studying PMMA/Graphite nanofillers (49).

2.4 Conclusion

Conductive PMMA/GNP ensembles were prepared by in situ polymerization of the monomer in the presence of graphite nanoplatelets. The electrical conductivity and dielectric properties of the materials were measured via the four-probe method and a network analyzer. An electrical conductivity of 10^{-4} S/cm and dielectric loss factor of 10^{-6} were obtained for the ensemble with 5 wt% GNP. The results showed that the electrical behavior of PMMA/GNP ensembles can be described well by percolation theory. Both the conductivity and dielectric loss factor were greatly enhanced near the percolation threshold. Due to the plentiful pores and the high aspect ratio of GNPs, molecular chains of polymers could easily penetrate into the pores by adsorp-

tion mechanisms. The unique structure of graphite nanoplatelets has a great effect on forming conducting network in PMMA matrix and improves both electrical and dielectric properties significantly.

CHAPTER 3

GRAPHENE-BASED FET STRUCTURE: MODELING FET CHARACTERISTICS FOR AN APTAMER-BASED ANALYTE SENSOR

3.1 Introduction

Graphene have been the subjects of research ever since the fabrication of monolayer graphene in 2004 (50). Its unique electrical and mechanical properties have resulted in efforts underlying a wide range of applications such as graphene-based nanocomposites and graphene-based FET structures (51; 52; 53). In addition to its electronic properties, graphene exhibits ballistic transport of electrons and holes on the sub-micron scale (54), which makes it a promising candidate for next-generation nanoelectronic devices (51).

Aptamers are artificial short DNA or RNA molecules, which perform as receptors for binding to targets of interest such as proteins, cells, DNA, inorganic ions, and small molecules with high specificity (55). Aptamers are usually selected from combinatorial libraries of synthetic nucleic acids by a process of adsorption, recovery and amplification coined SELEX for systematic evolution of ligands by exponential enrichment (56). An aptamer-based analyte sensor is a device converting a biological or chemical response into an electric signal.

In this chapter, a graphene-based FET-like aptamer sensor is modelled. The aptamer modified with methylene-blue (MB) is used as a conformational change reporter. 1-pyrenebutanoic acid, succinimidyl ester is used as a linker molecule to noncovalently bind the aptamer to the

graphene surface by the pyrene group. The graphene in these structures exhibits p-type semiconductor behavior due to residual hydroxyl groups. Electron trapping on the graphene surface is studied and a sheet charge capacitance model is established to explain the observed voltage shift in the I-V characteristics of the FET structure.

3.2 Theory and Model

3.2.1 Electron trapping on graphene surface

It is known that electrical contacts to a graphene surface typically exhibit high resistance (57; 58; 59). This is possibly due to the weak electron conduction on the interface. The electronic structure and the weak van der Waals binding cause relatively small matrix elements for electrons to cross the interface (57). Figure 6 shows the Brillouin zone and Fermi-level points of graphene. A simple tight-binding computation yields a spectrum with two Fermi points located at $\overrightarrow{k_1}$ = -2$\overrightarrow{g_1}$/3-$\overrightarrow{g_2}$/3 and $\overrightarrow{k_2}$ = -$\overrightarrow{k_1}$, which are just the corners of the two dimensional Brillouin zone (60). In order to have good conduction there must be states near the Fermi level that extend through both sides of the interface. If the Fermi level states do not overlap at the interface, there can be no extended states and thus no transfer of electrons. Another possible factor is that the conduction on the interface may be forbidden by the wave vector conservation or the Bloch symmetry of electrons. A perfect graphene sheet has one electron per carbon in the π orbital. In methylene blue molecules, π-electronic structure with C_{2v} symmetry is also the major contributor to the nonlinear polarizability (61). When the target molecule is present, MB undergoes a conformational change and could bend in all directions. If the wavevectors do

not overlap in the same direction, it is very likely that the electrons contributed by MB will be trapped on the graphene surface.

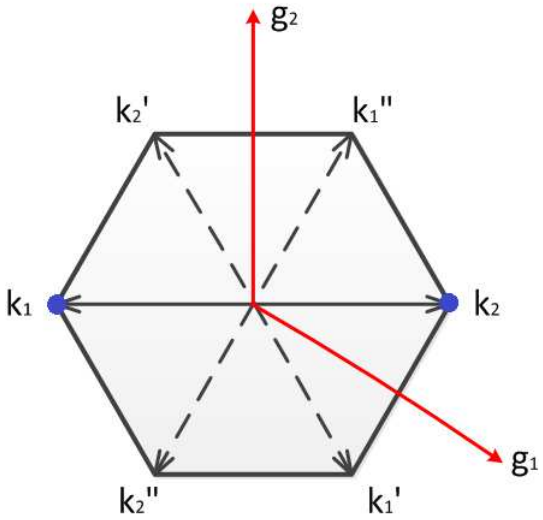

Figure 6. Two-dimensional Brillouin zone of graphene and Fermi-level points.

3.2.2 Charge sheet capacitance model of graphene-based FET analyte sensor

3.2.2.1 Graphene-based p-type MOSFET model

Graphene has a unique electronic structure with a zero gap and quasiparticles behaving like massless Dirac fermions. A graphene sheet has one electron per carbon in the π-levels and the

Fermi level is between the two symmetrical bands. However, band-structure calculations reveils that the electronic structure of a single graphene plane is not strictly symmetrical in energy. This asymmetry of electron-hole can shift the energy of the states localized near impurities above or below the Fermi level (62).

Graphene synthesized by different processing method could lead to different electronic behavior in the graphene-based FET structure. Researchers have reported the observation of p-type behavior of graphene in the FET structure (63; 64; 65). This may due to the residual hydroxyl groups inhibiting the n-type behavior of electrons. It had been well documented that hydroxyl groups can inhibit the electrons from functioning as free carriers in silicon FETs (63; 66). Other researcher have also reported that the electronic structure of graphene on SiO_2 strongly depends on the surface polarity and interface geometry. In the case of an interface geometry where graphene is weakly bonded to an O-polar surface, graphene behaves as p-doped material (67). Based on the above analysis, we conduct the device characteristic calculations for p-type MOSFET model.

3.2.2.2 Charge sheet capacitance model

When the cocaine molecule is present, cocaine aptamers with methylene blue at the end will fold to form a three way junction. The methylene blue could provide excess electron charges to the graphene surface and in turn modify the I-V characteristics of the P-MOS model.

After the inversion layer is formed, the net charge carrier density will reduce due to the external excess charge. We can assume,

$$Q(Net) = Q_p - Q_{ext}, \tag{3.1}$$

where Q_p is the inversion charge and Q_{ext} is the extra electron charge provided by methylene blue. At equilibrium, the inversion layer charge in MOS-C will balances the charge added to the gate when V_G exceeds V_T. Therefore,

$$Q_p = -Q_{gate} \cong -C_o \Delta V_G = -C_o(V_G - V_T). \tag{3.2}$$

The external charge Q_{ext} depends on the concentration of cocaine. More cocaine molecules near the structure will cause more aptamers to make the conformational change, leading to additional electron charge at the surface.

To analyze the current-voltage behavior, we begin with

$$J_p = q\mu_p p\mathscr{E} - qD_p \nabla p. \tag{3.3}$$

Since the current flow in the conducting channel is almost exclusively in one direction (taken to be y direction), and since the diffusion current is usually negligible compared with more numerous carriers at a certain point, we could simplify the equation to

$$J_p = q\mu_p p\mathscr{E} = -q\mu_p p\frac{d\phi}{dy}, \tag{3.4}$$

where μ_p is the mobility of holes. Thus the current flow in the conduction channel may be expressed as

$$I_D = \int\int J_p dxdz \tag{3.5}$$

$$= -\int\int q\mu_p \frac{d\phi}{dy} dxdz = (-Z\frac{d\phi}{dy})\int_0^{x_c(y)} \mu_p(x,y)p(x,y)dx. \tag{3.6}$$

The effective mobility $\overline{\mu_p}$ may be defined as

$$\overline{\mu_p} = -\frac{q}{Q_{N(y)}}\int_0^{x_c(y)} \mu_p(x,y)p(x,y)dx. \tag{3.7}$$

Equation 6 may be further simplified as

$$I_D = -Z\overline{\mu_p}Q_p\frac{d\phi}{dy}, \tag{3.8}$$

where Q_p is the positive charge/cm^2 in the channel. Integrating I_D over the length of channel gives

$$\int_0^L I_D dy = I_D L = -Z \int_0^{-V_D} \overline{\mu_p} Q_p d\phi \tag{3.9}$$

$$I_D = -\frac{Z\overline{\mu_p}}{L} \int_0^{-V_D} Q_p d\phi. \tag{3.10}$$

In our model, due to the existence of excess electron charges provided by methylene blue,

$$Q_p(Net) = -C_0(V_G - V_T - \phi) - Q_{ext}, \tag{3.11}$$

where Q_{ext} is the trapped external charge from MB. From the two equations above, we obtain the I_D-V_D relation

$$I_D = \frac{Z\overline{\mu_p}C_0}{L}[(V_G - V_T)V_D - \frac{{V_D}^2}{2}] - \frac{Z\overline{\mu_p}V_D}{L}Q_{ext}. \tag{3.12}$$

3.3 Results and Discussion

3.3.1 Graphene-based FET Structure

We use cocaine as a target to test our graphene-FET aptamer sensor as shown in Figure 7. The aptamer modified with methylene-blue (MB) as engineered by Baker et al. (68) is used as a conformational change reporter. MB is an electron donor, while chemical oxidation-reduction synthesized graphene usually shows p-type semiconductor behavior with holes as

carriers. 1-pyrenebutanoic acid, succinimidyl ester (merchandise name: P130) as the red dot in Figure 7, is used as linker molecule to noncovalently bind the aptamer to the graphene surface by the pyrene group as in the protocol used for Carbon nanotube (69). The pyrene group, being highly aromatic in nature, is known to interact strongly with the basal plane of graphite via π-stacking, due to the overlapping of π bonds between aromatic side chains. The cocaine aptamer is about 2-nm in length with 30 bases, which is less than the Debye length (70) that defined as the typical distance required for screening the surplus charge by the mobile carrier present in a material. When the target molecule, cocaine, is present, the aptamer will undergo a conformation change and thus change the distance between the MB and the graphene surface. When the MB approaches the surface, it can provide excess electrons that changed the I-V characteristics of the graphene-FET as described previously.

3.3.2 Comparison of the model with the measured data

After device fabrication, cocaine initially dispersed in water is sensed. Figure 8 shows the current-voltage relationship in the FET structure. The original I_{SD} curve shows typical p-type graphene behavior and agrees well with previous results (65; 71), where the current decreases with increasing V_{BG} from -60 V to 60 V. After the cocaine aptamer is immobilized on the graphene surface, the I_{SD} current experiences a current decrease from 20.5 μA to 15.8 μA at -60 V and from 19.7 μA to 15 μA at 60 V. Further, when cocaine is present, the I_{SD} continues to reduce with increasing concentration of cocaine. At -60 V, the current drops from 15.8 μA to 10.5 μA, 9.7 μA, and 9.4 μA for cocaine solution of 0, 1 μM, 10 μM, and 100 μM, respectively; while at 60 V, the corresponding currents are 15.0 μA, 10.0 μA, 9.2μA, and 9.0

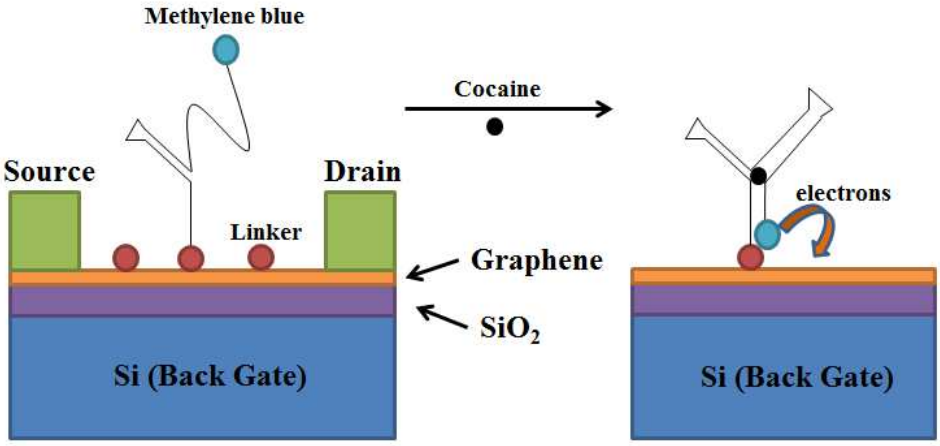

Figure 7. Scheme of graphene-based FET structure for detecting charges from MB close to the graphene surface.

μA, respectively. The current decrease or conductance reduction is very stable in the variable V_{BG}, as it is expected from the charge sheet capacitance model. The device appears to be saturated up to 100 μM with a nonlinear current drop to about 45% of original value.

These phenomena can be well explained by the charge sheet capacitance model. As can be seen from the device scheme in Figure 7, when the graphene surface is exposed to cocaine and causes the conformation change of the aptamers, MB will approach the graphene surface and contribute electrons. While ox-re graphene is a p-type semiconductor with hole as carriers, the electrons from MB will lower the carrier concentration of graphene, and thus lower the conductance. Increasing the cocaine concentration will cause more aptamers to make the configurational change, and lead to more electrons being trapped on the surface. The current

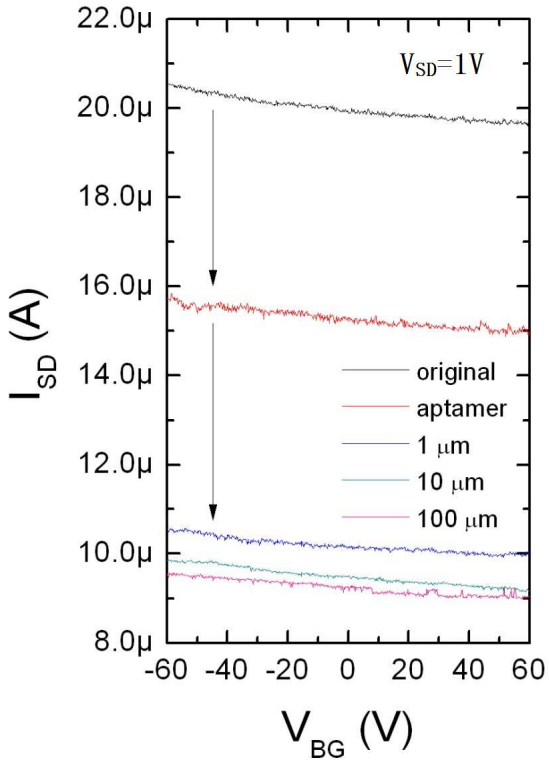

Figure 8. I_{SD} versus V_{BG} curves of different conditions: original device, aptamer-immobilized, 1 M, 10 M, and 100 M cocaine-in-water-tested with the arrow indication.

or conductance exhibits a stable decrease in the variable V_{BG}. This is because the structure will act like a capacitor as explained in the model. The charges trapped at the interface will be compensated in the graphene which acts as p-type semiconductor. If charges have been trapped on the surface the threshold voltage will be shifted. The change in threshold voltage depends on the amount of electron charge trapped at the interface. The relationship between trapped

electron charges and shift of voltage may be written as: $\Delta V_{TH} C_0 = Q_{ext}$. Thus, electrons contributed by MB will directly lead to a shift of voltage.

Similar results had been reported for unfunctionalized graphene (65; 71), where a larger current decrease was observed. It is to be noted that the slope of I_{SD}-V_{BG} curve is related to the dimensions of the FET device (Z/L) in the triode regime. Taking the derivative of Equation 12,

$$\frac{dI_D}{dV_G} = \frac{Z\overline{\mu_p}C_0}{L}, \tag{3.13}$$

In our structure the length of the channel (15 μm) is twice the length (7 μm) in Dr. Yang's device, and the width may also be relatively smaller due to rough (non-parallel) electrodes. Thus the conductance decreasing rate in our device is relatively lower.

3.4 Conclusion

In this chapter, the characteristics of a graphene-based FET aptamer sensor have been modelled and compared with experiment. The device performs as a signal-off sensor and detects cocaine in the micromole concentration regime. The graphene-based FET structures exhibits typical p-type semiconductor behavior due to residual hydroxyl groups. Methylene blue can serve as electron donor to the graphene FET structure. Electron trapping on graphene surface is studied as well as the I-V characteristics of the FET structure. A shift in voltage is clearly observed as expected in the sheet charge capacitance model. These results demonstrate the effectiveness of the model to understand the use of this device as a sensor of molecular analytes.

CHAPTER 4

SURFACE-ENHANCED RAMAN SPECTROSCOPY AS A TOOL FOR CHARACTERIZING NANOSTRUCTURES CONTAINING MOLECULAR COMPONENTS

4.1 Introduction

Raman spectroscopy, which is based on inelastic scattering of light that interacts with phonons or molecular vibrations in the nanostructure, has been widely used to identify chemical and biological molecules. Surface-Enhanced Raman Spectroscopy (SERS) greatly enhanced the sensitivity of conventional Raman spectroscopy by a factor of $\geqq 10^6$ through the use of a plasmon-generating substrate. In this chapter we investigated the use of Raman spectroscopy/SERS to verify that synthesized nanostructures contain active molecular components critical to their functioning. In particular, we uses SERS to identify the signature spectrum of Methylene Blue (MB) and uses standard Raman spectroscopy to verify the fictionalization of a DNA aptamer terminated with MB.

4.2 Raman spectroscopy and SERS

Raman spectroscopy has been widely used to identify chemical and biological molecules for its ability to differentiate the spectral fingerprint of molecules, resulting in very high multiplexing capabilities. Raman spectroscopy is based on inelastic scattering of light that interacts with phonons or molecular vibrations in the nanostructure. The potential for remote sensing makes

Raman spectroscopy especially useful in sensor development. Since the Raman spectra contains information on the vibrational modes or phonons that's between and within molecules, each single molecule have its unique spectra. The conventional Raman spectroscopy suffers from a small scattering cross section. Surface-enhanced Raman Spectroscopy (SERS) technique greatly enhances the sensitivity of standard Raman spectroscopy.

Surface-enhanced Raman scattering (SERS) is a technique used to enhance the signal strength during Raman scattering. SERS is based on the use of substrates that has nanometer scale geometries of metals (such as silver, gold, and copper) on top of it. Among the metals, silver has the best performance for frequencies in the visible range and has the lowest damping rate. When excited by incident laser light, the metals produce surface plasmons in the form of oscillating electrons. SERS enhancement of Raman signals can be explained by the electromagnetic behaviors inside nanostructures (72). Briefy, laser light excites the electrons and generate strong localized surface plasmons which can enhance the Raman scattering effect of molecules near metal surface. The Raman signal is proportional to the number of molecules in the field of detection and the Raman cross section. With the help of SERS, fewer molecules are required to obtain the same Raman signal.

SERS can give comprehensive information about the target structure, its vibrational and electronic properties, and even orientation of a single molecule absorbed on metallic nanomaterial surface (73). A variety of matallic nanomaterial have been proved to be SERS-active, such as metal electrodes, colloidal metal films and metal coated nano-arrays (74). Among those nanostructures, silver has been found to exhibit good Raman response and give strong enhance-

ment effect due to its large dielectric constant and high thermal conductivity (75). Methylene blue (MB) is a widely studied dye in photodynamic reactions. The electrical and mechanical properties of MB had been investigated with different electrodes such as gold, graphite and silver. It have been shown that MB adsorbed on silver electrodes can produce very strong SERS signal (76). Techniques for fabricating SERS substrate including nanosphere lithography to produce a silver film over nanospheres (77) and silver nanorod (AgNR) arrays fabricated with the Oblique Angle Deposition (OAD) technique (78).

Standard Raman spectroscopy and SERS are used to investigate the functionalization process of synthesized nanostructures contain active molecular components. In particular, we uses Surface-enhanced Raman spectroscopy to identify the signature spectrum of Methylene Blue (MB) and compares the enhancement factor of different concentration. Standard Raman spectroscopy is also used to verify the functionalization of a DNA aptamer terminated with MB to the surface of a graphene-based FET structure.

4.3 Experiment

SERS substrates consisting of silver nanorod arrays were prepared by oblique angle deposition (OAD). OAD is a physical vapor deposition technique that produce SERS-active nanorod arrays of varying aspect ratios. Compared with other technique such as electron-beam lithography which is expensive and requires elaborate preparation protocols, OAD can be performed on any standard thermal evaporation system equipped with a holder capable of rotation in the polar direction.

The substrate was first created by applying a titanium adhesion layer and a 200 nm silver film base layer onto a piece of glass slide. In order to gorw silver nanorods, the substrate was positioned such that it formed such that the vapor from the source is incident on the substrate close to the grazing angle (79). This specific angle results in the growth of the nanorod arrays aligned in a specific direction on the substrate. During this process, the length, diameter, and the aspect ratio of the nanorods can be controlled. A higher aspect ratio lead to a larger enhancement factor (80). The enhancement factor is also affected by the lateral arrangement of the silver nanorods. The more overlapping between nanorods, the greater the SERS signal (78; 80; 81). The silver nanorods used here were fabricated by our collaborator from University of Georgia using a custom-designed electron-beam/sputtering evaporation system. More details are described in previously published papers (82).

Methylene Blue is selected as the probing molecule in order to determine the SERS activity. MB solutions were diluted in deionized H_2O to reach concentrations of 1.5 mM and 0.15 mM, respectively. A drop of each concentration of MB was pipette onto on SERS substrate and left dry at room temperature. The samples were then incubated overnight. Before making the measurements, each sample was rinsed using Milli-Q water and dried with compressed air.

All SERS samples were then imaged with a Renishaw Ramascope 2000 spectrometer using 0.23 mW power and 514 nm excitation wavelength (Ar^+ -ion laser). The system was equipped with a high performance microscope and CCD camera. The spectra were recorded using a specialized microscope objective (Olympus, 50X) to focus the laser on the sample and to collect the backscattered signal. The power density for each sample was 13,000 W/cm^2 and the acqui-

sition time was 30 seconds. It is to be noted that background signal was subtracted to obtain the signal spectrum of target molecule. Standard Raman spectra was obtained by placing a 1.5 mM drop of the sample on a silicon substrate and imaging with 2.3 mW laser power.

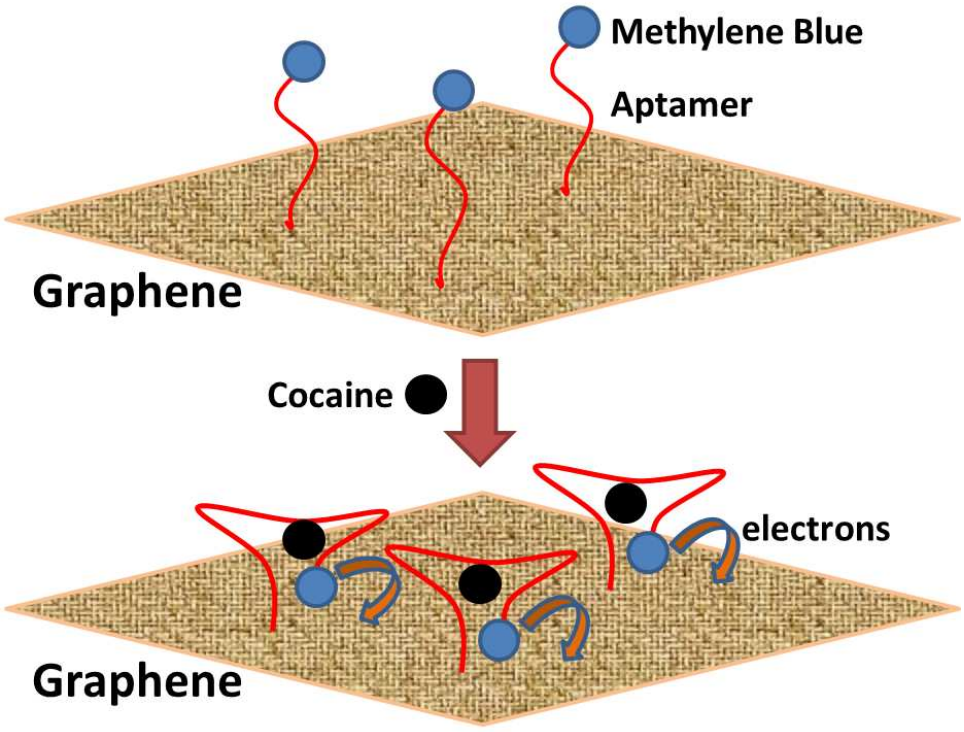

Figure 9. Scheme of graphene-based structure for detecting charges from MB close to the graphene surface.

Another sample was prepared by attaching cocaine aptamer terminated with MB to the surface of a graphene-based structure as shown in Figure 9. Standard Raman spectroscopy is used to identify the immobilization of the DNA aptamer. MB is used as an electron donor in the structure, while chemical oxidation-reduction synthesized graphene usually shows p-type semiconductor behavior with holes as carriers. The cocaine aptamer is about 30 bases. When the target molecule, cocaine, is present, the aptamer will undergo a conformation change and thus change the distance between the MB and the graphene surface. By comparing the Raman spectra before and after adding the cocaine to the structure, we could obtain information of the immobilization process of DNA aptamer as well as the characterization of sample surface.

4.4 Results and Discussion

The SERS spectra of MB absorbed on silver nanorods substrate with different concentrations of 1.5 mM and 0.15 mM are presented in Figure 10. Standard Raman spectra of 1.5 mM MB drop on Si substrate are also showed in the figure as a comparison of SERS enhancement factor. The main absorption peaks of MB solution are located at 293 (not shown), 610 and 656 nm (83), which are all away from the excitation wavelength of 514 nm. Thus the resonant Raman effect is expected to be very weak. Standard Raman spectrum indicates that many Raman scattering signal of MB without enhancement is too weak to be observed. This is due to the small amount of Raman scattering from the material deposited on the Si surface. Spectrum (b) shows visible enhancement activity from the silver nanoparticles with only 0.15 mM concentration of MB. When increasing the Methylene Blue concentration to 1.5 mM as in spectra (a), the Raman intensity increases drastically. The characteristic peak of MB at about 1628 cm^{-1}, which has

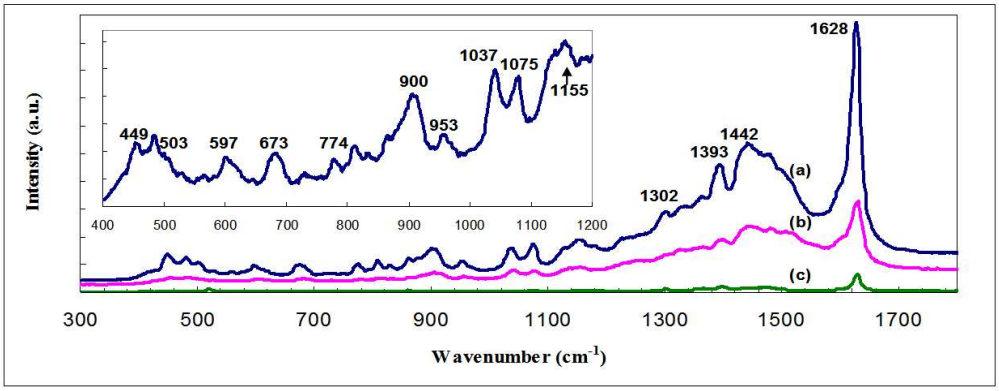

Figure 10. SERS spectrum of MB with different concentration of (a) 1.5 mM, (b) 0.15 mM, and (c) standard Raman spectrum of 1.5 mM MB drop on Si Substrate. An inset shows the enhanced SERS spectrum of (a) from 400 to 1200 (cm^{-1}) with main peaks identified.

been assigned to the C-C stretching and C-N-C skeletal bending (83), was well observed. An inset shows the enhanced SERS spectrum of (a) from 400 cm^{-1} to 1200 cm^{-1} with main peaks identified. This proves that the SERS substrate has the ability to reveal molecular details of the MB molecules absorbed on substrate surface.

Figure 11 shows the whole Raman spectra of the same graphene sheet of original graphene, aptamer-immobilization, and cocaine-tested, respectively. These three Raman spectra are identical and agree with the typical Raman spectrum of multiple layer graphene. The processed Raman spectra on the right side of Figure 11 are produced by subtracting between the two spectra on the left. Since most DNA Raman shifts are in area of 1000 cm^{-1} to 1800 cm^{-1} (84),

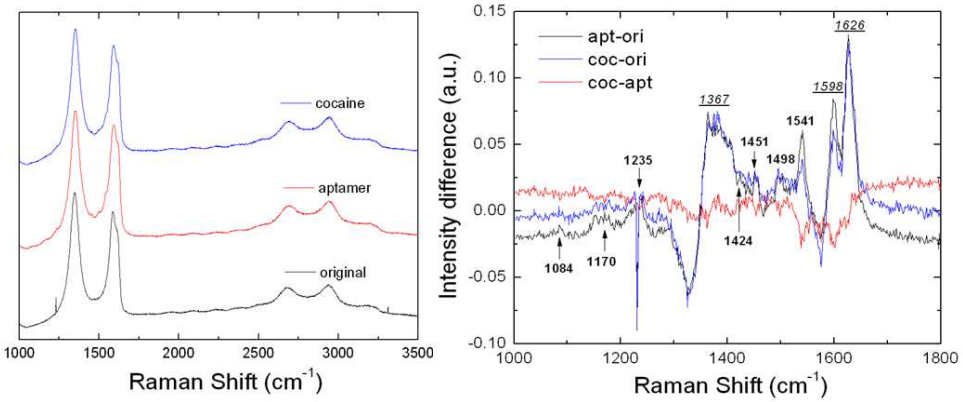

Figure 11. (a) Raman spectrum of the structure and (b) substrate deducted Raman spectra of original, aptamer-attached, and cocaine-tested structure with peaks identified.

we focus on this specific area. The reduced Raman spectrum labeled as "apt-ori" displays the difference between the spectrum of the original and the aptamer-immobilized graphene sheet. The peaks include typical Raman peaks of graphene sheet, like 1367 cm^{-1} for D peak, 1598 cm^{-1} for G peak. The other noted peaks are typical peaks of DNA, which have been carefully studied in Ref. (84; 85).

The Raman shifts and peak assignments of the main vibrational modes observed in SERS spectra and standard Raman spectra are listed in Table 1. The observed MB band positions are in well agreement with previously published results (83; 86; 87; 88). Some of the bands in SERS spectra shift a little in position as compared to the corresponding bands in standard Raman spectrum. Such as the main peak of 1626 cm^{-1} in standard Raman spectrum shifted to

TABLE I

RAMAN SHIFTS AND PEAK ASSIGNMENTS FOR MB, DNA APTAMER AND GRAPHENE

Methylene Blue (cm^{-1})	Band assignment
1628	$\nu(CC)$ ring+$\nu(CNC)$ ring
1442	$\nu_{asym}(C-N)$
1393	$\alpha(C-H)$
1302	$\nu(C-C)$ ring
1155	$\beta(C-H)$
1075	$\nu_{asym}(C-S-C)$
1037	$\beta(C-H)$
673	$\gamma(C-H)$
449	$\delta(C-N-C)$
DNA or Graphene (cm^{-1})	**Band assignment**
1598	G peak of graphene
1541	base Thymine
1498	$NC-NC$ stretching in guanine
1424	stretching of $C-N$ bonds in Thymine
1367	D peak of graphene
1235	ring stretching mode in Thymine
1084	symmetric stretching mode of PO_2^- backbone

1628 cm^{-1} in SERS spectrum. This is maybe due to the fact that methylene blue molecules are chemisorbed on the silver nanorods particles surface (89), and chemical effects cause the shift in SERS signal. Raman spectra of the cocaine aptamer with MB shows typical peaks of both DNA and MB, which proves that the aptamers have been successfully attached to the graphene surface.

4.5 Conclusion

Raman spectroscopy and SERS are used to verify that synthesized nanostructures contain active molecular components critical to their functioning. The SERS spectrum of MB was observed clearly with all the main peaks consistent with previously published results. The SERS technique provides significant enhancement in obtaining molecular details of methylene blue molecule. Raman spectra of the cocaine aptamer with MB shows typical peaks of both DNA and MB, which proves that the aptamers have been successfully attached to the structure surface. These results demonstrate the effectiveness of the silver nanorod SERS substrate in obtaining the Raman spectra of chemical and biological samples as well as the advantage of using Raman spectroscopy to investigate biochemical reaction in nanostructure.

CHAPTER 5

OPTICAL DETECTION OF LEAD AND POTASSIUM IONS USING A QUANTUM-DOT-BASED APTAMER NANOSENSOR

Quantum-dot (QD) based nanosensors can be used to detect a wide range of molecules. We examined a nanosensor comprised of thrombin binding aptamer (TBA) with 700NC InGaP QD on the 5' terminus and an Au nanoparticle quencher on the 3' terminus. Both K^+ and Pb^{2+} bind to TBA, resulting in a conformational change that brings the Au quencher closer to the QD. Photolumescence measurements indicated a decrease in fluorescence corresponding to an increase in either K^+ or Pb^{2+} concentration. For healthy blood serum K^+ concentrations (3.5-5 mM), the beacon exhibited 15-17% quenching efficiency. Pb^{2+} concentration of 0.48 μM, the threshold for toxicity in serum, yielded 14% quenching. The beacon's ability to detect changes in ion levels in a critical range of concentrations can make it an effective diagnostic tool.

5.1 Introduction

5.1.1 Quantum dots

In recent years, quantum dots (QDs) have gained popularity in a wide variety of scientific applications. Quantum dots (QDs) are nanocrystalline semiconductor materials with size ranging from a few nanometers to a few hundred nanometers. Quantum dots have properties between the bulk and the molecular forms of matter. Direct bandgap QDs, in particular, are useful as detecting agents due to their extremely short excited-state lifetime (sub-nanosecond)

and their ability to fluoresce in response to incident light. When excited with laser light equal to or greater in energy than the QD's bandgap, an electron moves to the conduction band, leaving a hole in the valence band. The created electron-hole pair is called an exciton. Recombination of the electron and hole results in the release of a photon.

The optical properties of quantum dots are highly dependent on the shape, size and composition of the quantum dot due to a phenomenon called quantum confinement. Electrons have discrete energy levels inside quantum dots. Energy transition is only allowed between certain levels. Due to this unique nature, the absorption spectra for quantum dots exhibit a series of overlapping peaks. Short wavelength corresponding to large peaks. The wavelength of the first exciton peak is called the absorption onset. Incoming light with a wavelength longer than the first exciton transition will not be able to be absorbed by the quantum dot. The peak emission wavelength is Gaussian shape and occurs at a wavelength larger than the lowest energy exciton peak. It is to be noted that the peak emission wavelength is independent of the excitation light wavelength. The bandwidth of quantum dots' emission spectra is defined as the Full width at half maximum (FWHM). FWHM is mostly caused by inhomogeneous spectral emission broadening due to inhomogeneous size distribution of the quantum dot.

Previous imaging techniques use natural molecules that fluoresce, such as proteins and organic dyes that are found in jellyfish or fireflies. There are several disadvantages of using these natural molecules. For example, each of the dyes emit light over a certain range of wavelength, and their spectra overlap. This makes the use of multiple dyes to tag different biomolecules at the same time very difficult. In addition, the fluorescence of dyes also tends to

fade away quickly in a short time. Quantum dots, on the other hand, are brighter, live longer than dyes, have a much narrower emission peaks and broader excitation range (90).

QDs can also be used as fluorescence probes for labeling cellular proteins thanks to its ability to preserve enzyme activity. Since QDs have a 420-fold increase over the organic, labeling with QDs is much more photo-stable than with organic dyes. In addition, the photo-stability and high achievable signal-to-noise ratio achievable makes quantum dot an ideal probe for single molecule tracking studies. Thanks to the extremely high photo-stability of QDs, real-time monitoring and tracking of intracellular processes over long periods of time become possible.

5.1.2 Quantum-dot-based biosensors

QDs can be synthesized with a number of organic linkers and bound to biological structures for optical detection. Nanocrystal quantum dots are emerging as a new class of fluorescent labels for in vivo cellular imaging. With an inert layer of surface coating, the nanocrystals QDs are less toxic than organic dyes. In recent years, non-toxic biocompatible QDs, such as the indium gallium phosphate (InGaP) QDs that we used, became available as an alternative to the widely-used cadmium-based QDs (91).

Gold nanoparticles were used as quenchers. When a QD is excited in close proximity to an Au nanoparticle, the energy emitted by the QD is transferred to the Au nanoparticle instead of being emitted as a photon. This process is known as nanosurface energy transfer (NSET). The broad absorption spectrum of Au nanoparticles (around 300-800 nm) (92) makes them effective at quenching light in a wide range of wavelengths, therefore, they can be used with a variety of QDs. Quenching efficiency for NSET is proportional to $1/d^4$, where d is the distance between

donor and quencher (93). NSET has an advantage over the more widely-known fluorescent resonance energy transfer (FRET), which is largely limited by the dipole-dipole interactions between the donor and acceptor. Because the dipole moments of the donor and acceptor have to be close to parallel in order for FRET to occur (94), the quenching typically does not occur if the donor and acceptor are farther than 10 nm apart, and quenching efficiency is proportional to $1/d^6$ (95). Instead of dipole-dipole interactions, NSET relies on the interaction between the donor dipole's electromagnetic field and the conduction electrons on the surface of the acceptor (94). As a result, NSET can occur from as far as 22 nm, more than double the FRET distance (95).

Thrombin binding aptamer (TBA) is the final component of the beacon discussed in this chapter. DNA aptamers are man-made single stranded oligonucleotides that bind to a specific target. Unlike traditional antibodies, they can be produced in vitro, have higher specificity, and can be easily modified with functional groups for conjugation to other structures (96; 97). In addition to binding to the peptide thrombin, TBA has been shown to bind to potassium and lead (98; 99; 100). Upon binding, the 15-base DNA strand undergoes a conformational change and forms a quadraplex structure, thereby bringing the two termini closer together (101). Thus, a QD linked to an Au nanoparticle via TBA will undergo quenching in the presence of target ions due to the increased proximity of the Au nanoparticle (Figure 12).

In this chapter, we investigates the effectiveness of a QD-TBA-Au beacon in optically detecting Pb^{2+} and K^{+}. Both ions play an important role in human health, so accurately detecting their levels is vital for diagnostic purposes. The CDC has defined the blood Pb^{2+} level of

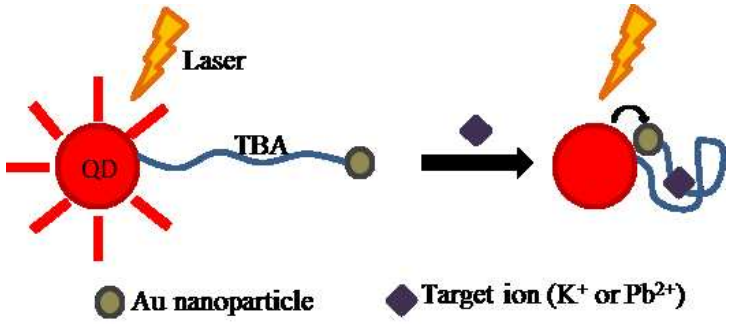

Figure 12. K^+ and Pb^{2+} detection via a QD-TBA-Au sensor. In the presence of the target ions, the QD's fluorescence is quenched by the Au nanoparticle.

10 g/dL as the threshold for toxicity (102). Exposure to Pb^{2+} can cause intellectual deficits in children and has been correlated with higher incidence of cancer and circulatory disease in adults (102). K^+ plays a key role in the generation of action potentials and cell signaling, and both excess and deficiency of K^+ can have serious detrimental effects (103). Therefore, a simple optical sensor for K^+ and Pb^{2+} would be beneficial to human health and diagnostics.

5.2 Experiment

TBA with 5' amino and 3' thiol modifications (5'-/Amino C12/GGTTGGTGTGGTTGG/Thiol C6 SS/-3') was purchased from Biosearch Technologies, Inc. (Novato, CA) and dissolved in Tris ethylenediamine tetraethyl acetate (EDTA) buffer (10 mM Tris, 1 mM EDTA, pH 7.4) to a concentration of 100 μM. A total of 2 nmoles (20 μL) of TBA was used in the synthesis. To reduce the dithiol groups, 6 μL of Bond-Breaker TCEP solution (Pierce Biotechnology, Rockford, IL) was incubated with the TBA for 30 minutes at room temperature.

Monomaleimido Nanogold particles 1.4 nm in diameter were obtained from Nanoprobes (Yaphank, NY). One vial (6 nmoles) was dissolved in 100 μL deionized H20 and added to the TBA. Reduced dithiols will bind to the malemido group on the Au particles to produce Au-TBA conjugates. A 3:1 Au:TBA ratio was used in this synthesis to ensure the presence of Au on each TBA molecule, since excess Au can be easily filtered out later in the conjugation process. After a 2-hour incubation at room temperature, the solution was centrifuged twice at 3,000x g for 15 minutes using a 3K Nanosep molecular weight cutoff (MWCO) device (Life Sciences, Ann Arbor, MI) to remove TCEP. Carboxyl-functionalized eFluor 700NC InGaP QDs were purchased from eBiosceince, Inc. (San Diego, CA). There are an estimated 10 carboxyl groups per QD, so 0.2 nmoles of QDs was used in the conjugation to attain a 1:10 QD:DNA ratio. The QDs were buffer exchanged into 0.1 M 2-(N-morpholino)ethanesulfonic acid (MES) buffer by centrifuging for 5 minutes at 10,000x g in a 100K MWCO device.

Carboxyl groups on the QDs were activated with 50 μg 1-Ethyl-3-[3-dimethylamino propyl] carbodiimide hydrochloride (EDC) (Pierce Biotechnology, Rockford, IL) and 50 μg N-hydroxysulfo-succinimide (Sulfo-NHS) (Pierce Biotechnology, Rockford, IL). After 30 minutes of gentle spinning at room temperature, the solution was centrifuged twice at 3,000x g for 15 minutes to filter out EDC and Sulfo-NHS. The same MWCO device was used to buffer exchange the solution into low sodium PBS. The Au-TBA conjugate was then added to the activated QDs, and the solution was spun gently for 2 hours at room temperature. After 2 hours, the conjugate was again centrifuged 3,000x g for 15 minutes 3 times to remove unbound TBA and Au. Ideally, the

resulting composite would be a complete beacon containing a QD with 1-10 Au-TBA complexes attached.

Photoluminescence (PL) spectra were obtained using a USB4000 Ocean Optics (Dundelin, FL) spectrometer with a 380 nm LED as the excitation source. Potassium chloride (Fischer Chemicals, Fair Lawn, NJ) solutions at concentrations of 10 μM to 100 mM were prepared via dilution in deionized water. Similarly, lead(II) chloride (Sigma-Aldrich, St. Louis, MO) solutions at concentrations of 50 nm to 10 mM were prepared by dissolving Pb(II)Cl in deionized water. A beacon concentration of 10 μM was used in each case.

5.3 Results and Discussion

These data confirm previously-published results on the use of similar optical beacons as Pb^{2+} and K^{+} sensors (98; 99; 104). In addition, we tested the beacon in a wider range of target ion concentrations than previously attempted (98; 99).

Figure 13 shows the changes in PL intensity with increases in target ion concentration. The fact that intensity decreases as target concentration increases confirms the formation of TBA's quadruplex structure and the resulting quenching of the QDs by the Au nanoparticles. Quenching efficiency (Figure 14) was calculated using the equation $E=(I_0-I)/I_0$, where E is the quenching efficiency, I_0 is the PL intensity in the absence of any target ions, and I is the PL intensity at a specific target ion concentration. The sensor appears to be more sensitive to Pb^{2+}, showing a 31% quenching efficiency for 1 mM Pb^{2+}, versus only 17% for the same concentration of K^{+}. In addition, the rate of increase of quenching efficiency with respect to concentration is greater for Pb^{2+} than K^{+}.

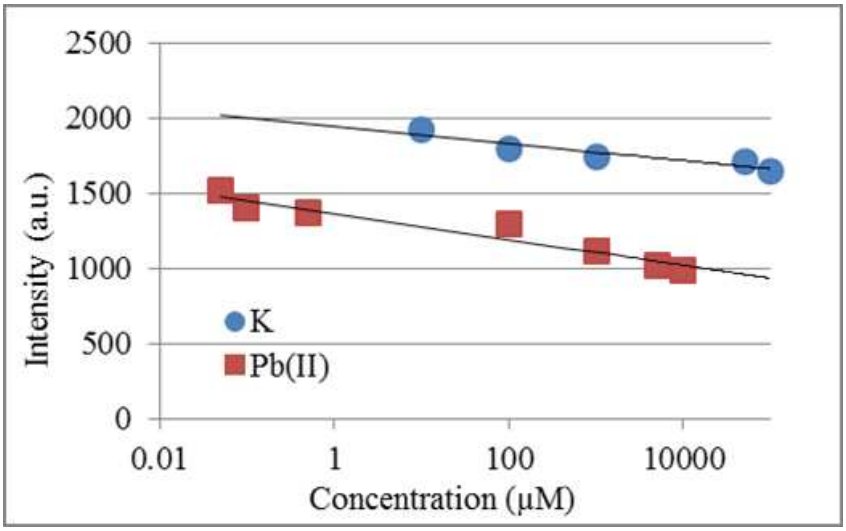

Figure 13. PL intensity at various concentrations of K^+ and Pb^{2+}.

The beacon presented can potentially be used as a diagnostic tool. According to the laboratory test reference values provided by the Massachusetts General Hospital, blood serum K^+ levels in a healthy person are 3.5-5 mmol/L (105). The beacon's quenching efficiency for 3.5 mM and 5 mM K^+, extrapolated from Figure 14, is 17% and 15%, respectively. Assuming that 10 μM beacon solution would be used to test blood serum, <15% quenching would indicate hyperkalemia (elevated K^+ levels) and >17% quenching would indicate hypokalemia (low K^+ levels).

Massachusetts General Hospital lists safe serum Pb^{2+} levels as 0.5-1 μmol/L (105). Similarly, the CDC defines the blood Pb^{2+} level of 10 g/dL as the threshold for toxicity (102), which corresponds to 0.48 μM. Based on the trendline in Figure 14, 0.48 μM Pb^{2+} will yield

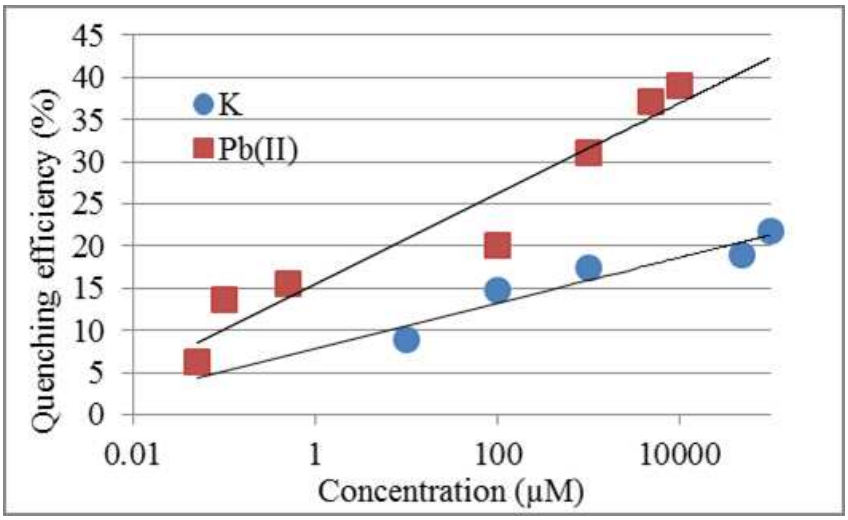

Figure 14. Quenching efficiency at various concentrations of K^+ and Pb^{2+}.

14% quenching. Thus, if this beacon is used to test blood for elevated lead levels, >14% quenching would be cause for concern. It is also worth noting that the PL intensity of the beacon without target ions present is 81% lower than the PL intensity of unconjugated QDs of the same concentration (Figure 15). This implies that even without TBA's conformational change, the QDs in solution are in close enough proximity to Au nanoparticles for NSET to occur. However, this does not present a serious problem since, as seen in Figure 13 and 14, the beacon is still sensitive to nM and μM concentrations of target ions. This intensity decrease is also significant considering that the peak emission of the QDs used here is around 690 nm, which is on the edge of Au's absorption spectrum. Thus, it is likely that the intensity decrease would be even greater for lower-wavelength QDs.

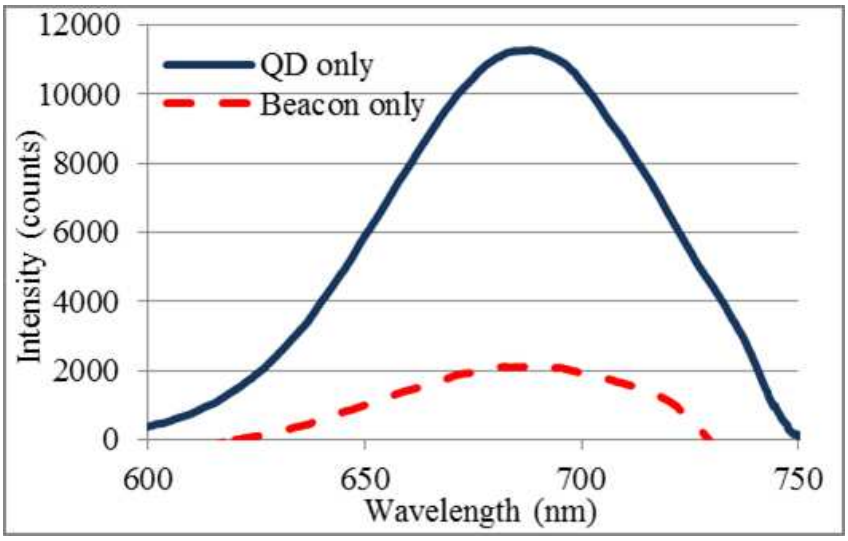

Figure 15. Difference in PL intensity between plain QDs and beacon in the absence of target ions. A concentration of 10 μM was used for both plain QDs and beacon.

5.4 Conclusion

The QD-TBA-Au optical nanosensor can effectively detect changes in K^+ and Pb^{2+} concentrations in a range critical for human health. PL can be used to measure NSET-induced quenching, from which the ion concentration can be estimated. Its effectiveness and simple design make this sensor a valuable tool for K^+ and Pb^{2+} detection.

CHAPTER 6

GRAPHENE- AND APTAMER-BASED ELECTROCHEMICAL BIOSENSOR

We investigated the effectiveness of a graphene- and aptamer-based FET-like sensor in detecting lead and potassium ions. The sensor consists of a graphene-covered Si/SiO_2 wafer with thrombin binding aptamer (TBA) attached to the graphene layer and terminated by a methylene blue (MB) molecule. K^+ and Pb^{2+} both bind to TBA and cause a conformational change, which results in MB moving closer to the graphene surface and donating an electron. Thus, the abundance of K^+ and Pb^{2+} can be determined by monitoring the current across the source and drain channel. Device transfer curves were obtained with ambipolar field effect observed. Current readings were taken for K^+ concentrations of 100 μM to 50 mM and Pb^{2+} concentrations of 10 μM to 10 mM. As expected, I_d decreased as ion concentration increased. In addition, there was a negative shift in V_{Dirac} in response to increased ion concentration.

6.1 Introduction

In recent years, there have been an increasing number of studies on highly sensitive, reagentless, electrochemical biosensors based on DNA aptamers (106; 107). While the number of aptamer-based studies is increasing, nucleic-acid-based aptamers have still been relatively insufficiently explored compared to other selectively binding molecules such as the larger amino-acid-based antibodies. In this study, a relatively small aptamer (only 15 active DNA bases) -

that we have investigated in background studies addressing its basic conformational and selectivity properties (108; 109; 110) - known as the thrombin binding aptamer (TBA), is used as the active molecular sensing element in conjunction with a graphene-based substrate. These aptamer-based electrochemical sensors potentially provide a nanoscale-sensing alternative for the detection of an extremely wide range of targets including ions, small molecules, nucleic acids, proteins, and even cells, tissues, and organisms (107). Carbon nanotubes (CNTs), can be visualized as crystalline carbon sheets rolled into cylindrical tubes, have attracted great attention in the development of FET-like nanosensors (111). However, it is difficult to separate metallic CNTs from semiconducting CNTs, which is a major engineering issue in fabricating pure carbon nanotubes. In addition, due to its small interface, it is a great challenge to manipulate CNTs during device fabrication when only a few of CNTs are used. On the other hand, a flat alternative to the carbon nanotube, graphene, has large surface area and unique ambipolar characteristics which made it an effective platform for biomolecular sensing. Compared with oxide reduced graphene or exfoliated graphene, graphene films grown by chemical vapor deposition (CVD) are much better candidates for device fabrication as a result of to their large area, uniformity, and better reproducibility (112).

Graphene-based FETs have been demonstrated for real-time detection of various metal ions in solution. Chen et al. (113) reported FETs using thermally reduced graphene oxide as sensing substrate to detect mercury ions. Sudibya et al. (114) used micropatterned reduced graphene oxide film as sensing channel to detect different metal ions in aqueous solutions. Typically, these graphene-based FET sensors use graphene-based materials as the conducting or sensing

channel, and monitor the electric signal change during the interaction between graphene and target chemicals. In this chapter, we demonstrated a biosensor with a graphene-based FET structure using DNA aptamers as receptors for one of the smallest possible analytes - ions. Accordingly, our study explores a prototype nanosensor for a unique array of nanosensors for small-analyte detection based on a versatile graphene platform using small molecular recognition units.

Aptamers are man-made DNA, RNA, or peptide segments which display high binding efficiency to specific targets (115). Compared with other recognition elements such as antibodies, aptamers have a wide range of advantages such as smaller size, chemical stability, and the ability to be manufactured in vitro without the need for living organisms (115). We used the thrombin binding aptamer (TBA), a 15-base single-stranded DNA molecule that, in addition to the peptide thrombin, has been shown to bind to potassium and lead (116; 117). The selectivity is due to specific cations' ability to interact with the guanines on the aptamer and stabilize the G-quadraplex structure (118). To confirm this selective binding, TBA has been previously tested against many other metal ions, including Li, Na, Mg, Ca, Cu, Ni, Zn, Cd, Cr, Al, Hg, Au, and Fe (117; 119). These previously reported selectivity tests were taken into account. Hg^{2+} has been shown to bind to symmetrical thymines on TBA, causing the aptamer to fold into a T-Hg^{2+}-T hairpin structure (119). In this study, we focused on the detection of G-quadraplex-stabilizing ions, namely K^{+} and Pb^{2+}.

The configuration of the graphene-based biomolecular sensor is schematically shown in Figure 16. The aptamers are connected to the graphene surface via a linker molecule (Pyrene Cap

Phosphoramidite®, Glen Research) which has a pyrene group for binding to graphene and is connected to the aptamer by phosphoramidite chemistry. Due to the overlapping of -bonds between aromatic side chains, the pyrene group can be firmly attached to the graphene surface through - stacking. Methylene blue (MB) is an electron-rich electrochemical redox indicator that functions as an electron donor. Upon binding to a target molecule, the 15-base TBA, which consists of several deoxyguanosine (G) units, undergoes a conformational change and forms a G-quadraplex structure (120). This conformational change brings the methylene blue (MB) molecules that are attached to the other end of TBA closer to the graphene surface and produce a readily detectable Faradaic current. This electron transfer is inhibited before the conformational change because TBA is in "standing" position and the electron-tunneling distance is much larger. Similar aptamer-MB structure had been reported by other researchers (121; 122; 123).

We investigated the effectiveness of the FET-like biosensor in detecting Pb^{2+} and K^{+} ions. Accurate detection of these ions is important for environmental reasons and human health. Pb^{2+} is a common byproduct of industrial waste and has been known to cause significant health problems including developmental deficits in children and, in some cases, early death in adults (124). K^{+} is an essential ion that regulates cell signaling in living organisms, and human blood serum K^{+} levels above or below the 3.5 mM - 5 mM range are cause for concern (125). Thus, an effective sensor for Pb^{2+} and K^{+} would be greatly beneficial.

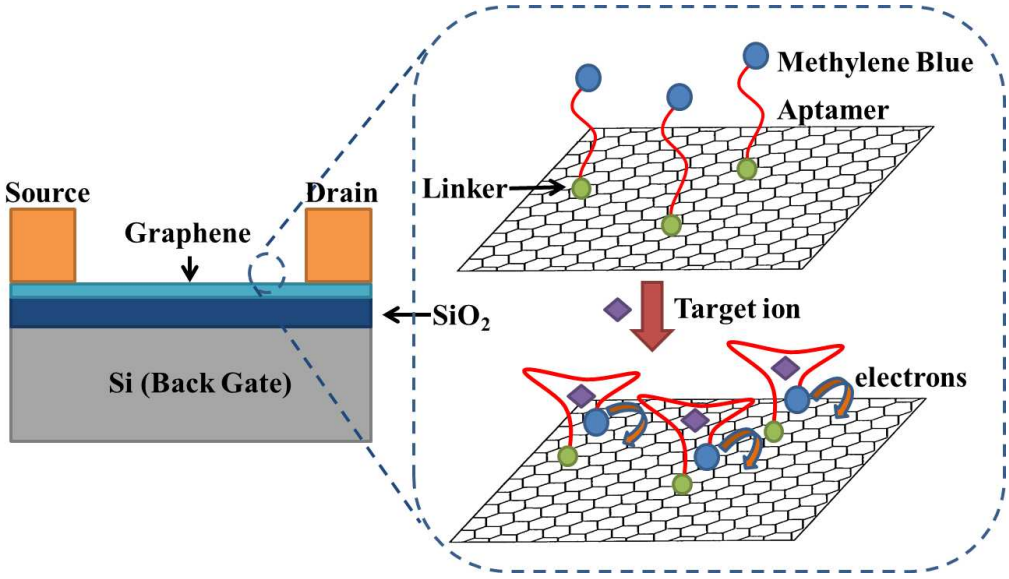

Figure 16. Schematic illustration of Graphene-based biosensor.

6.2 Experiment

6.2.1 Fabrication of graphene-based biosensor

Graphene samples were originally grown on copper foil using low pressure chemical vapor deposition (LPCVD). Growths were performed at 1025 deg C for 30 minutes at 0.5 - 0.6 Torr pressure using hydrogen and methane as the carrier and carbon feedstock gases. In order to transfer the graphene sheet to a Si/SiO_2 substrate, the copper foil was coated with PMMA and went through an O2 plasma ashing process to remove backside graphene. After wet etching of the copper foil, the PMMA/graphene sheet was transferred onto an n++ Si substrate coated with 296 nm of SiO_2. The thickness of the Si wafer is 525 μm. Finally, PMMA was removed by

soaking in chloroform. Raman characterization of the graphene after transfer was performed using a Renishaw inVia Raman microscope with an excitation laser wavelength of 514 nm. In lieu of precise mapping, Raman spectra were taken at multiple points over a 60 x 40 μm area and the characteristic graphene peaks were fitted using the Lorentz peak approximation. Based on analysis of the Raman data, the graphene films consisted mostly of single layer graphene with small amounts of bilayer graphene present (9 - 11%).

The FET-like structure was fabricated on the graphene surface using optical lithography. 45-nm thick gold and 5-nm thick chromium were deposited on the graphene sheet as source and drain electrodes using electron beam evaporation. Source and drain were patterned by photoresist mask and chemical etching technique. Owing to the large size and good uniformity of the CVD grown graphene film, we were able to fabricate 9 identical electrodes on the same substrate available for multi-channel detection. This also enabled us to perform device characteristic measurements and device performance comparisons without being affected by artifacts from discrete flakes. The length and width of the channel were both set to be 2 mm for ease-of-use as a biomolecule sensor in the future. The Si wafer was degenerately doped with a conductivity of 0.005 Ωcm and used as the global backgate.

6.2.2 Synthesis of control structures for optical experiments

The ability of DNA to bind to graphene via a pyrene group was tested by first synthesizing a control structure, where methylene blue was replaced with a fluorescent quantum dot (QD). Since QDs are fluorescent, the binding of TBA-QD to graphene can be confirmed via optical microscopy. Thus, the control structures were used in the preliminary step of the

experiment to confirm the aptamer's ability to bind to graphene via the pyrene group. TBA with 5' pyrene and 3' amine modifications (5'-/Pyrene /GGTTGGTGTGGTTGG/AminoC12/-3') was purchased from Biosearch Technologies, Inc. (Novato, CA). Carboxyl-functionalized eFluor 700NC InGaP QDs were purchased from eBioscience, Inc. (San Diego, CA) and conjugated to TBA. To achieve the conjugation, the QDs were first exchanged into 0.1 M 2-(N-morpholino)ethanesulfonic acid (MES) buffer via a 100K Nanosep® molecular weight cutoff (MWCO) device (Life Sciences, Ann Arbor, MI). Carboxyl groups on the QDs were activated with 1-Ethyl-3-(3-dimethylamino propyl)carbodiimide hydrochloride (EDC) (Pierce Biotechnology, Rockford, IL) and N-hydroxysulfosuccinimide (Sulfo-NHS) (Pierce Biotechnology, Rockford, IL). A 100K MWCO device was then used to filter out EDC and Sulfo-NHS and buffer exchange the solution into low-sodium phosphate-buffered saline (PBS). TBA was added to the activated QDs at a 1:10 QD:TBA ratio, and the mixture was spun gently at room temperature for 2 hours. Finally, the conjugate was filtered using a 100K MWCO device to remove unbound TBA.

Before attaching the TBA-QD conjugate to graphene, the wafer was washed in acetone and deionized H_2O. TBA-QD was buffer exchanged into anhydrous dimethylformamide (DMF) (Sigma-Aldrich, St. Louis, MO). A 15 μM drop was placed on the graphene and incubated for 2 hours. The wafer was then rinsed thoroughly with diH2O to remove unbound conjugates. Plain QDs were also incubated on the graphene using the concentration and procedure described above. The samples were viewed using Nikon Eclipse E600 microscope. Raman spectroscopy was also performed on the samples to verify the presence of DNA on the graphene.

6.2.3 Synthesis of FET-like Sensor with DNA and Methylene Blue

TBA with 5' pyrene and 3' methylene blue modifications (5'-/Pyrene /GGTTGGTGTG-GTTGG/Methylene Blue/-3') was purchased from Biosearch Technologies, Inc. (Novato, CA). A 15 μM drop of TBA in anhydrous DMF was placed on the wafer between two contacts and left to incubate for 2 hours. The wafer was then washed twice with diH_2O, to remove unbound TBA and leave only the TBA that is attached to graphene via pyrene linker. Pb(II)Cl_2, KCl, and NaCl were dissolved in diH2O to obtain solutions of various ion concentrations. 5-μL drops of ion solution were placed on the wafer on the spot occupied by TBA, and probes were placed on the adjacent contacts.

All electrical measurements were conducted at room temperature using a Precision Semiconductor Parameter Analyzer (Agilent, 4156B). In order to have better contact on the interface, a 8060 MicroManipulator Probing System was used to connect the Semiconductor Parameter Analyzer with the sample surface. The electrodes remain dry during all electrical measurements.

6.3 Results and Discussion

6.3.1 Optical verification of DNA-graphene bonding

Figure 17 shows the attachment of TBA-QD to graphene compared to plain QDs. Red fluorescence indicates the presence of QDs. The fluorescence intensity in Figure 17(b) is clearly higher than in Figure 17(d), demonstrating that a significant number of QD-TBA molecules remained on the graphene even after the wafer was rinsed with diH2O. Plain QDs, in contrast, were largely removed by the rinsing process consisting of two rinse cycles. In addition, the edge of the graphene flake is visible in Figure 16, and TBA-QD clearly binds to graphene only. These

results demonstrate that pyrene successfully binds to graphene and can be used as an effective linker for the FET-like sensor. Raman results (not shown) also confirm binding of TBA to graphene with the presence of several peaks in the 900-1600 cm^{-1} range, which is consistent with typical wavenumbers for DNA peaks (126). This proof of binding, obtained through the use of TBA-QD control structures, allowed us to proceed to the main part of the experiment - the FET-like sensor with TBA aptamer and methylene blue.

6.3.2 Device characteristic

As shown in Figure 18, the conductance of dry, unfunctionalized graphene-based FET-like devices resembles the ambipolar field effect in semiconductors. The source-drain voltage is set constant at 10 mV and 25 mV, respectively. Mathematical curve-fitting was used to remove noise. Conductivity increases with V_g on both sides of the minimum conductance point. The device transfer curves (drain current I_d vs. gate voltage V_g) of the multiple graphene-based structures were found to be quite reproducible. The minimum conductance points were always in the positive backgate voltages, between 50 V to 70 V. The standard deviation of the gate voltage for minimal conductance point under the drain voltage of 10 mV and 25 mV are 0.72 V and 0.60 V, respectively. The location of minimum conductance point or Dirac point can be used to monitor the doping state of the graphene film. The shift of Dirac point voltage (V_{Dirac}) from zero to large positive V_g indicates that the graphene behaves like a degenerately doped p-type semiconductor without electric field doping (at zero V_g). This shift is also found by other research groups and can be attributed to unintentional doping by absorbed water in ambient conditions (127) as well as impurities adsorbed to the graphene during the fabrication process

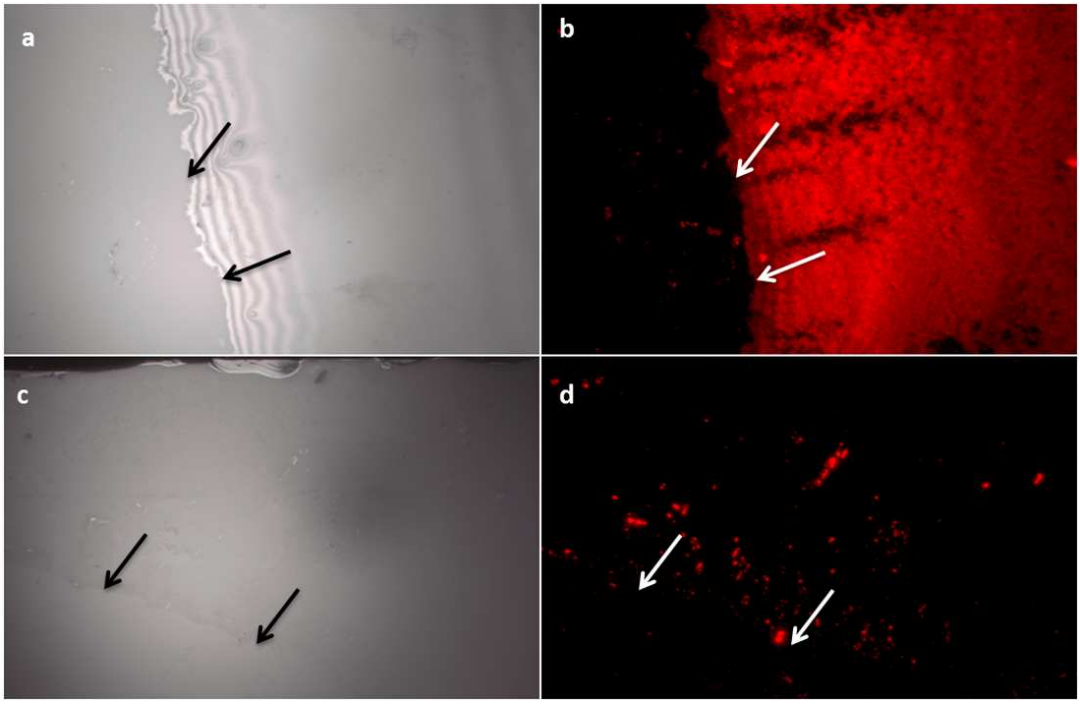

Figure 17. Microscope images of graphene wafers after 2-hour incubation with TBA-QD or plain QD after a thorough rinse with diH_2O. Arrows indicate the edge of the graphene flake. (a) Bright field image of graphene with TBA-QD. (b) Fluorescent image of graphene with TBA-QD. (c) Bright field image of graphene with plain QDs. (d) Fluorescent image of graphene with plain QDs.

(128). It is possible that the negatively-charged impurities originated from the transfer process on the SiO_2 substrates are trapped underneath graphene layer and lead to intrinsic p-doping effect in the graphene (129). The drain source currents (I_d) are in the range of 0.39-0.80 μA and 0.45-1.29 μA, respectively, and the current on-off ratio is about 2. We used the current change after introduction of ions as an indication of detecting target ions. Single layer graphene has

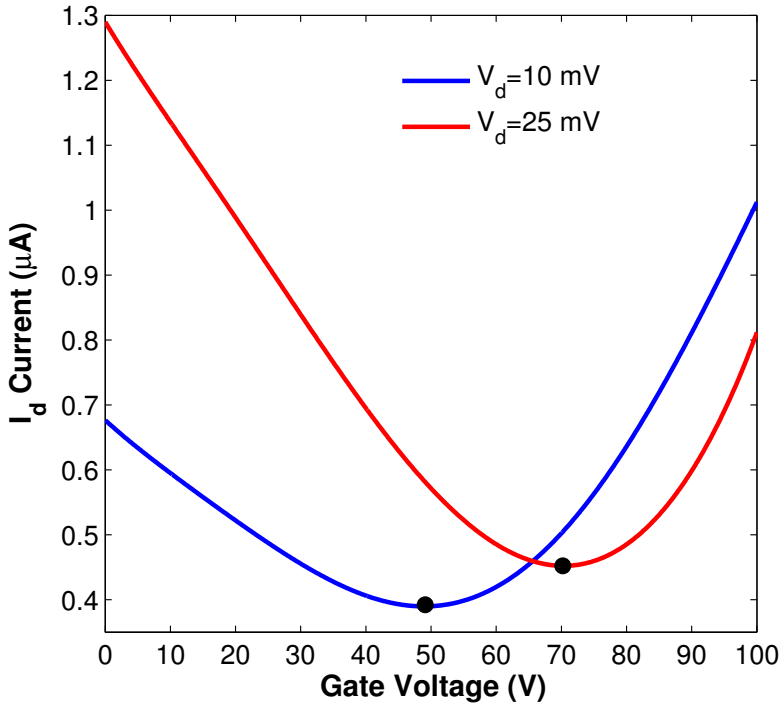

Figure 18. Device transfer curves of two graphene-based FET-like structures.

the unique electronic ability to be able to operate in both p-type and n-type conduction region (detailed discussion in section 3.3). The FET performance as shown in the device transfer curves allowed us to monitor the current changes in both conduction regions.

6.3.3 Graphene-based biomolecular sensor

The location of V_{Dirac} is sensitive to the immobilization of DNA aptamer structures. The green curve in Figure 19 shows the device transfer curve after the aptamer structure was at-

tached on the graphene surface. As compared to the blue curve from original device, the I_d current decreased and V_{Dirac} right-shifted after the aptamer structures were introduced to the device. This is possibly due to the noncovalent functionalization process of the DNA aptamer. Although the relatively weak - stacking or van der Waals interaction can preserve the superb physical properties of graphene, it has been demonstrated that functionalization with pyrene groups can cause V_{Dirac} to shift significantly towards the right, indicating a typical p-type doping behavior (130). Huang et al. also discovered a current decrease and right-shift after functionalizing graphene surface with linker molecules consisting pyrene groups (131).

In order to understand the use of this device as a biomolecular sensor, it is necessary to consider the underlying principles by which the graphene-based biosensor functions. Large-area-graphene transistors are known to have unique current-voltage transfer characteristics as shown in Figure 18. The transfer curve can be divided into two branches separated by the Dirac point which is the minimum conductance point. The type of carrier and carrier density in the channel are modulated by the potential difference between the gate and the channel. On the right side of the Dirac point where large positive gate voltages are applied, electrons accumulate and form an n-type conduction channel. On the left side of the Dirac point, negative gate voltage (compared to V_{Dirac}) lead to a p-type conduction channel where holes are the majority carrier.

As shown in Figure 19, the device transfer curve shifted after different concentrations of K^+ were added into the sensor. To be specific, after adding 100 μM concentration of K^+ (red curve), the current in the channel decreased in the range of 0 V - 51.1 V gate voltage. This is because the device is working in the p-type conduction region with holes as the majority

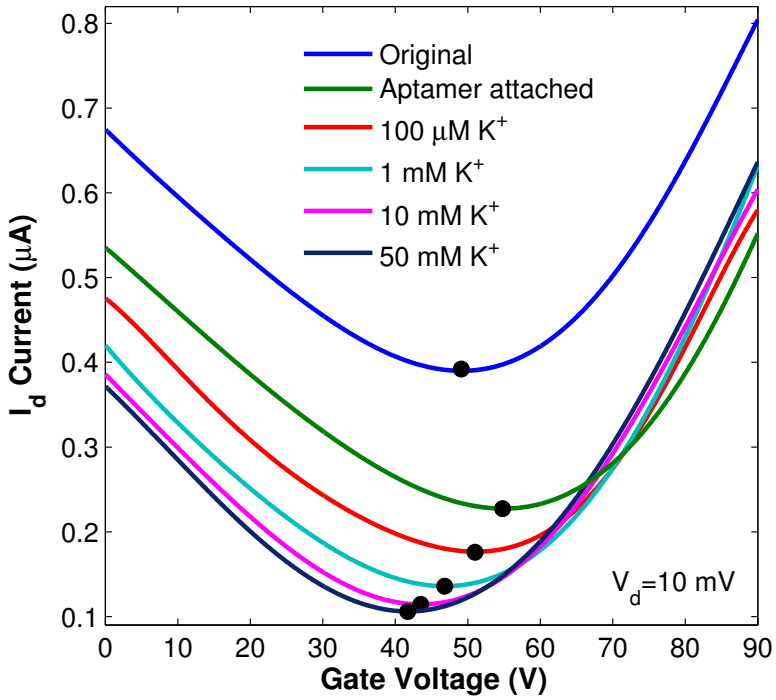

Figure 19. Device transfer curves of the original FET-like structure, the structure after aptamer attachment, and after adding different concentrations of K^+ ions.

carriers. When K^+ is introduced into the structure, aptamers undergo conformational change and bring MB close to the surface. The excess electrons transferred from MB will decrease the carrier concentration in the channel and cause a current decrease. On the other hand, when gate voltage is greater than V_{Dirac}, the device works in the n-type conduction region and the external electron charges will lead to an increase in carrier concentration as well as an increase in the current. This explains the rise of current after 51.1 V gate voltage. The current decrease

in the p-type conduction region and current increase in the n-type conduction region proves that we have successfully detected K^+ ions.

It's worth noting that aside from current change V_{Dirac} also shifted from 54.9 V (green curve) to 51.1 V (red curve). As discussed previously the left-shift of V_{Dirac} can be the result of the n-doping effect. Electrical contacts to a graphene surface have been found to exhibit high resistance (132). Weak electron conduction at the contact-graphene interface can cause the external electrons provided by methylene blue to be trapped on the graphene surface. It's likely that the electron transfer and electron accumulation induced an n-doping effect inside graphene. Similar negative shift of V_{Dirac} had been reported by Chen et al. after functionalizing graphene with short DNA strands (112). They attributed the n-doping effect to the interaction between graphene and electron-rich nucleobases in DNA molecules.

The transfer curve continues to shift with the increasing concentration of K^+. The minimum conduction current and V_{Dirac} position at different K^+ concentrations are shown in Table 1. After adding 50 mM of K^+, the minimum conduction current dropped by about 51.2%.

In order to investigate the effectiveness of the device in detecting Pb^{2+}, another graphene-based biosensor was fabricated with identical structure. Figure 20 shows the transfer curve changes with the increases in Pb^{2+} concentration. Similar changes have been observed as in the K^+ detection measurement, indicating consistent performance of the device.

Data for the minimum conduction current and V_{Dirac} position at different Pb^{2+} concentrations are shown in Table 2. The minimum conduction current dropped about 62.7% after adding 10 mM of Pb^{2+}.

TABLE II

V_{DIRAC} VOLTAGE AND MINIMUM CONDUCTION CURRENT AT DIFFERENT K^+ CONCENTRATIONS.

I_d at different conditions	V_{Dirac} (V)	Minimum conduction current (μA)
Original Device	49.2	0.3921
Aptamer structure attached	54.9	0.2272
100 μM K^+ added	51.1	0.1758
1 mM K^+ added	46.9	0.1370
10 mM K^+ added	43.6	0.1185
50 mM K^+ added	41.8	0.1109

TABLE III

V_{DIRAC} VOLTAGE AND MINIMUM CONDUCTION CURRENT AT DIFFERENT PB^{2+} CONCENTRATIONS.

I_d at different conditions	V_{Dirac} (V)	Minimum conduction current (μA)
Original Device	70.3	0.4522
Aptamer structure attached	74.1	0.2562
10 μM Pb^{2+} added	68.2	0.1673
100 μM Pb^{2+} added	63.1	0.1219
1 mM Pb^{2+} added	61.5	0.1003
10 mM Pb^{2+} added	59.9	0.0956

The sensor appears to be more sensitive to Pb^{2+}, showing a 62.7% signal decrease for 10 mM Pb^{2+}, versus 47.8% for the same concentration of K^+. In addition, adding as little as 10 μM of Pb^{2+} causes the signal to decrease about 35%, while it takes nearly 1 mM of K^+ to reach the same signal decrease. Based on the calibration curves depicting the relationship between minimum conduction current and target ion concentration (Figure 21), the sensor

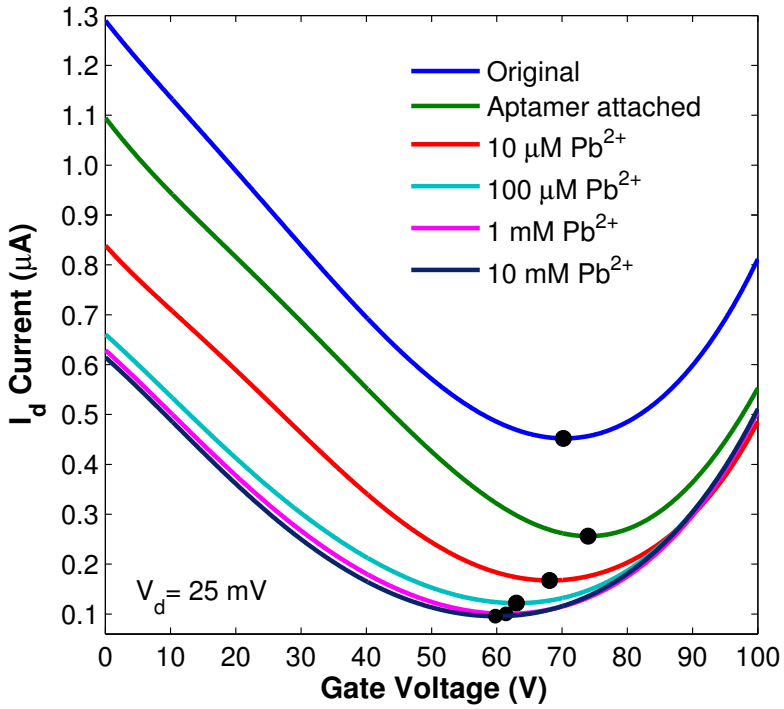

Figure 20. Device transfer curves of the original FET-like structure, the structure after aptamer attachment, and after adding different concentrations of Pb^{2+} ions.

appears to be more sensitive to K^+ concentrations below 10 mM and Pb^{2+} concentrations below 2 mM. For concentrations above these values, the signal saturates between 0.1 and 0.15 μA. Therefore, a linear trendline was fitted to the first three data points to estimate the sensor's sensitivity in its most sensitive region. According to the trendline equations, the sensitivity in this region is around 0.09 μA/mM for K^+ and 1.4 μA/mM for Pb^{2+}. The same calibration curves were used to estimate the detection limit. Based on the limitations of the Semiconductor

Parameter Analyzer used in the I-V measurements, the minimum detectable current change was determined, and the linear trendline equations were used to extrapolate the ion concentrations that would yield this current. The detection limit was thus calculated to be 27 μM for K^+ and 2 μM for Pb^{2+}.

The sensor's sensitivity is comparable to several commercially available sensors. The digital B-731 LAQUAtwin Compact Potassium Ion Meter (B-731) from HORIBA measures K^+ in 1-100 mM range. It has a resolution of 26 μM for K^+ concentrations in the 1-2.5 mM range, 256 μM in the 2.5-25 mM range, and 2.56 mM in the 25-100 mM range (133). While the sensor described in our work cannot detect such high concentrations, it has a lower detection limit and is more sensitive to lower concentrations of K^+ ions. HORIBA's Lead Ion Electrode (8008-10C) offers a measuring range of 10 μM-100 mM and an unknown resolution (134). This range is wider than the one offered by the sensor in our work, but, once again, the minimum detection limit is higher. Several digital lead sensing electrodes, such as Thermo Scientific's Orion Lead Electrode (9482BN) and PASCO Scientific's Lead Ion Sensitive Electrode (CI-6736) detect levels as low 1 μM and exhibit a semilogarithmic relationship where the voltage reading increases by 25-30 mV for every decade increase in Pb^{2+} concentration (135; 136). A 25 mV increase in voltage when the Pb^{2+} concentration increases from 1 to 10 μM translates to a higher sensitivity than the sensor described in our work. However, the detection limit is comparable. All the sensors described above function optimally at pH close to 7. To summarize, while our sensor cannot accurately detect concentrations on the mM scale, its lower detection limit is comparable with other commercially available sensors and the sensitivity is quite high at low

ion concentrations. Like other sensors, it functions best at neutral pH. Although one drawback is irretrievability of the sample, an advantage is the extremely small required sample volume (1 μL or less).

Buffer characteristics can affect the sensor's sensitivity. Hianik et al. reported on the effect of buffer pH and ionic strength on the binding efficiency of TBA to its target peptide, thrombin. A pH of 7.5 was determined to be optimal for binding, with the sensitivity decreasing significantly for higher and lower pH values. This is likely because the pH influences the structure of TBA's binding site, altering its binding ability. A pH of 7.5 is a convenient value for optimal sensor function, as it is close to physiological pH and the pH of water. Similarly, the sensitivity decreases with increasing NaCl concentrations, indicating that TBA functions optimally in buffers with low ionic strength. A likely explanation for this is that in high ionic strength buffers, the ions shield the negative charges on the DNA, making it harder for the aptamer to bind to its positively charged targets (137). It is therefore best to use the sensor for samples with minimal amounts of non-target ions. Nevertheless, previous work by our group has shown that TBA-based sensors undergo the binding-induced conformational change in a variety of buffers (108), including PBS buffer, TE (10 mM Tris, 1 mM EDTA, pH 8.0) buffer (116; 138), and physiological fluids such as urine (109).

The stability and selectivity of the biosensor was investigated by control experiments. Since the sensors are irreversible, it is not possible to conduct control experiments on the same functionalized sensors. Instead we designed three separate control experiments. In the first two experiments, K^+ and Pb^{2+} ions were introduced to the original graphene-based FET-like

structure without aptamers, respectively. In the third experiment, sodium ions were introduced to the aptamer-MB functionalized biosensor. Drain voltages in the control experiments were set at the same values as previous sensor experiments and gate voltages were 0V. To have a better look of the current change on control structures, we conducted control experiments with no gate voltage applied and monitored the time dependent response of drain current after the introductions of target ions. Figure 22 shows the normalized drain current as a function of time after the introduction of target ions with various concentrations. In order to have a good comparison, data from previous sensor experiments were plotted alongside with data from control experiments. Since the control experiments were conducted in separate control structures, the initial current values (before ion addition) were different in each experiment. Thus we normalized the currents with respect to their initial values so that after normalization all the currents start at 1. This normalization ensures that all three control experiment results are consistent and comparable. Without the TBA-MB structure, K^+ and Pb^{2+} ions were not able to cause sharp current decreases as they did in TBA-MB functionalized biosensors. Similarly, after adding sodium ions to the aptamer-MB functionalized biosensor, the drain current only exhibits a slight change, indicating a weak dependence of channel conductance with sodium concentrations. Comparing the lack of responses from control experiments and sharp current decrease from functionalized sensor measurements, we determined that the graphene-based biosensor is a good tool for the detection of both K^+ and Pb^{2+} ions.

6.4 Conclusion

We introduced a novel FET-like biosensor and proved its effectiveness in detecting K^+ and Pb^{2+} ions. It can potentially detect K^+ concentrations as low as 27 μM and 2μM concentrations of Pb^{2+}. The information in our paper is potentially useful for a whole class of nanosensors for detecting small analytes (much smaller than feasible with antibodies) based on a nanoscale graphene platform. Since detection of K^+ and Pb^{2+} at these concentrations is of the utmost importance for environmental and health reasons, the sensor can potentially be used in medical or industrial settings.

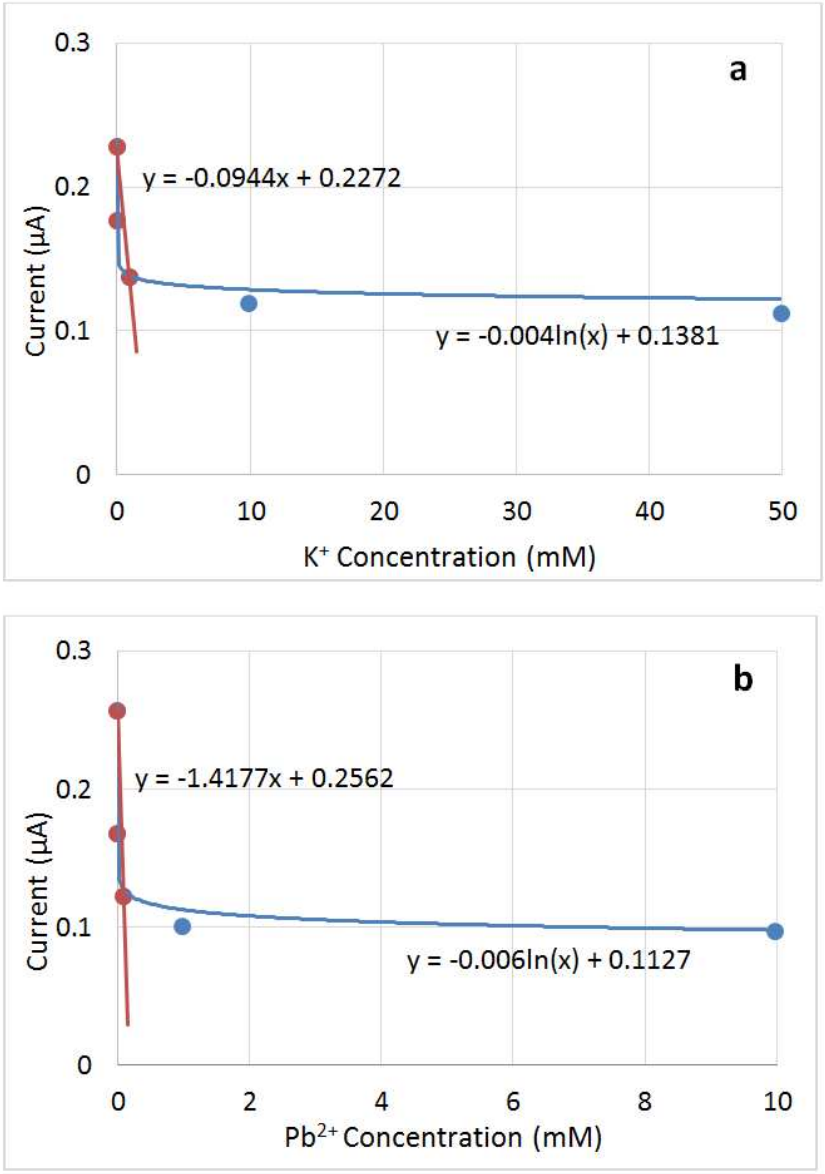

Figure 21. Calibration curves (relationship of minimum conduction current to K^+ (a) and Pb^{2+} (b) concentrations) with linear regression data. The logarithmic trendline characterizes the general relationship between current and concentration. A linear trendline was fitted to the first three data points to estimate the sensor's sensitivity in its most sensitive range.

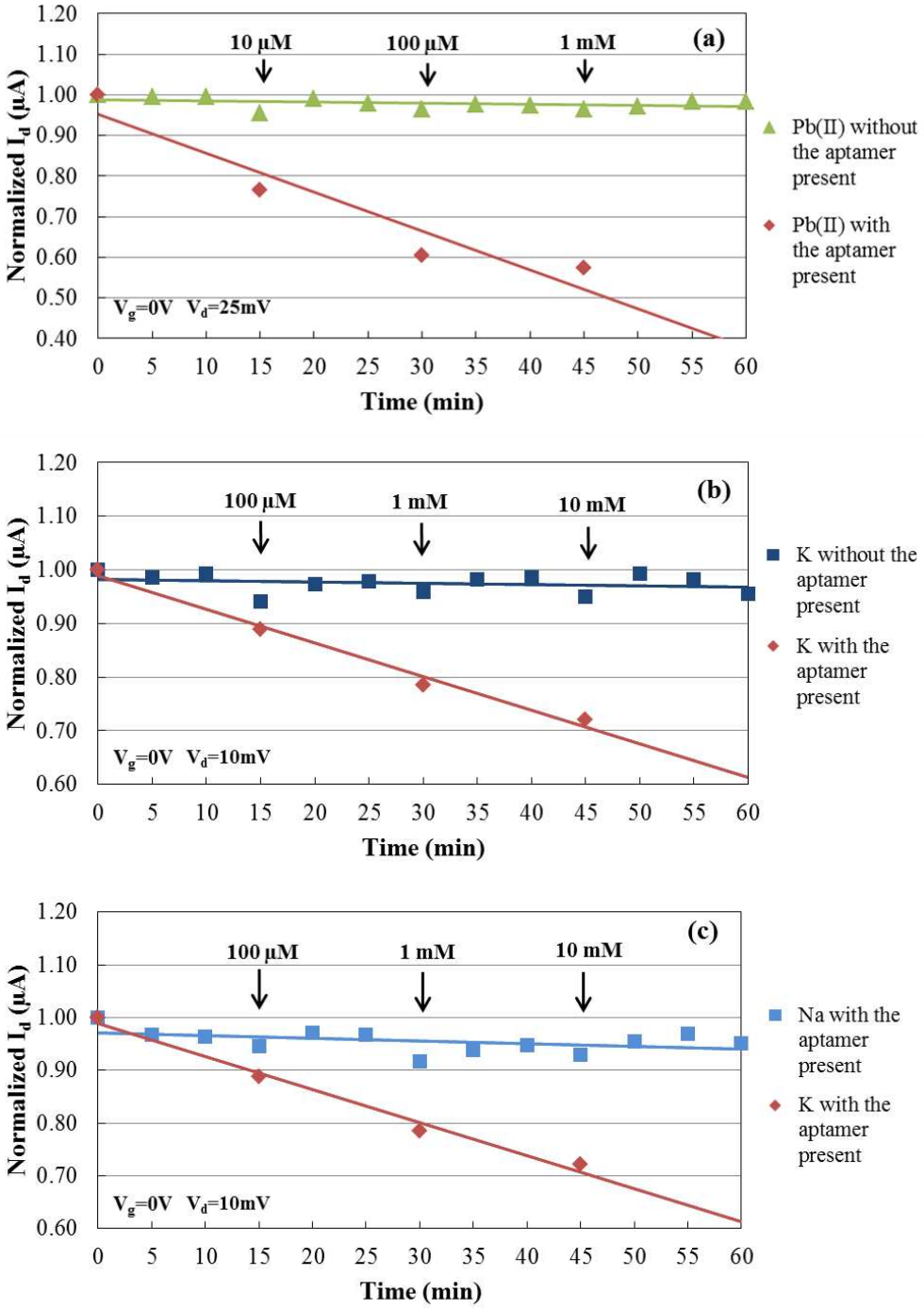

Figure 22. Drain current (I_d) response after the introduction of (a) Pb^{2+} ions without the aptamer present, (b) K^+ ions with the aptamer present and (c) Na^+ ions with the aptamer present. Data from previous sensor experiments were plotted alongside for comparison.

CHAPTER 7

CONCLUSION AND POSSIBLE FUTURE WORK

This thesis summarized our research in three major topics: polymer/graphene nanocomposites, graphene-based FET structure and its characteristics, and graphene- and aptamer-based nanostructure and its use in bimolecular sensing.

Study of polymer/graphene nanocomposites was discussed in Chapter 2. Conductive PMMA/GNP ensembles were prepared by in situ polymerization of the monomer in the presence of graphite nanoplatelets. An electrical conductivity of 10^{-4} S/cm and dielectric loss factor of 10^{-6} were obtained for the ensemble with 5 wt% GNP. The results showed that the electrical behavior of PMMA/GNP ensembles can be described well by percolation theory. Both the conductivity and dielectric loss factor were greatly enhanced near the percolation threshold. Due to the plentiful pores and the high aspect ratio of GNPs, molecular chains of polymers could easily penetrate into the pores by adsorption mechanisms. The unique structure of graphite nanoplatelets has a great effect on forming conducting network in PMMA matrix and improves both electrical and dielectric properties significantly.

In Chapter 3, the characteristics of a graphene-based FET aptamer sensor have been modelled and compared with experiment. The graphene-based FET structures exhibits typical p-type semiconductor behavior due to residual hydroxyl groups, and the device performs as a signal-off sensor and detects cocaine in the micromole concentration regime. Electron trapping on graphene surface is studied as well as the I-V characteristics of the FET structure. A shift

in voltage is clearly observed as expected in the sheet charge capacitance model. These results demonstrate the effectiveness of the model to understand the use of this device as a sensor of molecular analytes. In Chapter 4, We conducted Raman spectroscopy and SERS experiments to verify that synthesized nanostructures discussed in Chapter 3 contain active molecular components critical to their functioning. The SERS spectrum of MB was observed clearly with all the main peaks consistent with previously published results. The SERS technique provides significant enhancement in obtaining molecular details of methylene blue molecule. Raman spectra of the cocaine aptamer with MB shows typical peaks of both DNA and MB, which proves that the aptamers have been successfully attached to the structure surface. These results demonstrate the effectiveness of the silver nanorod SERS substrate in obtaining the Raman spectra of chemical and biological samples as well as the advantage of using Raman spectroscopy to investigate biochemical reaction in nanostructure.

In Chapter 5 and Chapter 6 we designed and fabricated two biosensors to detect potassium and lead ions. In Chapter 5 we dicussed a QD-TBA-Au optical nanosensor that can effectively detect changes in K^+ and Pb^{2+} concentrations in a range critical for human health. PL were used to measure NSET-induced quenching, from which the ion concentration can be estimated. Its effectiveness and simple design make this sensor a valuable tool for K^+ and Pb^{2+} detection. And in Chapter 6 we introduced a novel FET-like biosensor and proved its effectiveness in detecting K^+ and Pb^{2+} ions. It can potentially detect K^+ concentrations as low as 27 μM and 2μM concentrations of Pb^{2+}. Our study is potentially useful for a whole class of nanosensors for detecting small analytes (much smaller than feasible with antibodies) based on a nanoscale

graphene platform. Since detection of K^+ and Pb^{2+} at these concentrations is of the utmost importance for environmental and health reasons, the sensor can potentially be used in medical or industrial settings.

In the future, there are some aspects of the proposed grapene- and aptamer-based nanostructure that deserve further study. We can expand our techniques to other aptamers by simply replacing the TBA aptamer with other target aptamers. We can improve the stability of our sensor by varying the size of graphene sheets, aptamer concentrations, real-time response ability, and refreshing conditions. Finally we can also optimize the working condition of the sensor by replacing the Si-based back gate with a liquid gate on top of the graphene sample. This will significantly decrease the required gate voltage and increase the sensitivity of the sensor.

APPENDICES

Appendix A

ELSEVIER POLICY ON THESES AND DISSERTATIONS

Reprinted from Elsevier official website.

"Elsevier's Policy:

An author may use the PJA (Published Journal Articles) for personal use and internal institutional use (see below for definitions of these terms).

Personal use:

Use by an author in the author's classroom teaching (including distribution of copies, paper or electronic), distribution of copies to research colleagues for their personal use, use in a subsequent compilation of the author's works, inclusion in a thesis or dissertation, preparation of other derivative works such as extending the article to book-length form, or otherwise using or re-using portions or excerpts in other works (with full acknowledgment of the original publication of the article)."

Appendix B

IEEE POLICY ON THESES AND DISSERTATIONS

Reprinted from the Institute of Electrical and Electronics Engineers official website.

"Thesis / Dissertation Reuse:

The IEEE does not require individuals working on a thesis to obtain a formal reuse license, however, you may print out this statement to be used as a permission grant:

Requirements to be followed when using an entire IEEE copyrighted paper in a thesis:

1) The following IEEE copyright/ credit notice should be placed prominently in the references: [year of original publication] IEEE. Reprinted, with permission, from [author names, paper title, IEEE publication title, and month/year of publication] 2) Only the accepted version of an IEEE copyrighted paper can be used when posting the paper or your thesis on-line. 3) In placing the thesis on the author's university website, please display the following message in a prominent place on the website: In reference to IEEE copyrighted material which is used with permission in this thesis, the IEEE does not endorse any of [university/educational entity's name goes here]'s products or services. Internal or personal use of this material is permitted.

If applicable, University Microfilms and/or ProQuest Library, or the Archives of Canada may supply single copies of the dissertation."

Appendix C

AIP POLICY ON THESES AND DISSERTATIONS

Reprinted from the American Institute of Physics official website.

"AIP permits authors to include their published articles in a thesis or dissertation. It is understood that the thesis or dissertation may be published in print and/or electronic form and of fered for sale, as well as included in a university's repository. Formal permission from AIP is not needed. If the university requires written permission, however, we are happy to supply it."

Appendix D

IOP POLICY ON THESES AND DISSERTATIONS

Reprinted from IOPscience official website.

"Upon transfer of copyright, IOP and/or the copyright owner grants back to authors a number of rights. These include the right to copy the article for teaching purposes, and to include the article in research theses or dissertations. Please include citation details and for online use, a link to the Version of Record. IOP's permission will be required for commercial use of an article published as part of your thesis."

CITED LITERATURE

1. Moore, G.: Cramming more components onto integrated circuits. Electroncs Magazine, 38:114, 1965.

2. Schaller, R.: Moores law: past, present and future. IEEE Spectrum, 34:52, 1997.

3. S.Ijima: Helical microtubules of graphitic carbon. Nature, 354:56, 1991.

4. Novoselov, K., Geim, A., Morozov, S., Jiang, D., Zhang, Y., Dubonos, S., Grigorieva, I., and Firsov, A.: Electric field effect in atomically thin carbon films. Science, 306:666, 2004.

5. K.S.Novoselov, Jiang, D., Schedin, F., Booth, T., Khotkevich, V., Morozov, S., , and Geim, A.: Two-dimensional atomic crystals. Proceedings of the National Academy of Sciences of the United States of America, 102:10451, 2005.

6. Geim, A.: Graphene: Status and Prospects. Science, 324:1530, 2009.

7. Pinto, G. and Jimenez-Martin, A.: . Polym. Compos., 22:65, 2001.

8. Lu, J. R., Chen, X. F., Lu, W., and Chen, G.: . Eur. Polym. J., 42:1015, 2006.

9. Dong, Q., Zheng, Q., and Zhang, M.: . J. Mater. Sci., 41:3175, 2006.

10. Tang, Q. Y., Chan, Y. C., Wong, N. B., and Cheung, R.: . Polym. Int., 59:1240, 2010.

11. Peng, H.: . J. Am. Chem. Soc., 130:42, 2008.

12. Kalaitzidou, K., Fukushima, H., and Drzal, L. T.: . Carbon, 45:1446, 2007.

13. King, J. A., Tucker, K. W., Vogt, B. D., Weber, E., and Quan, C. L.: . Polym. Compos., 20:643–654, 1999.

14. Ramadurai, D., Geerpuram, D., Alexson, D., Dutta, M., Kotov, N., Tang, Z., and Stroscio, M.: . Superlattice Microst., 40:38, 2006.

CITED LITERATURE (Continued)

15. Sun, K., Stroscio, M., and Dutta, M.: . Superlattice Microst., 45(2):60, 2009.

16. Fim, F., Guterres, J. M., Basso, N. R. S., and Galland, G. B.: . J. Polym. Sci., 48:692, 2010.

17. Wu, X., Qi, S., He, J., and Duan, G.: . J. Mater. Sci., 45:483, 2010.

18. Novoselov, K. S., Geim, A. K., Morozov, S. V., Jiang, D., Zhang, Y., Dubonos, S., Grigorieva, I. V., and Firsov, A. A.: . Science, 306:666, 2004.

19. Geim, A. and Novoselov, K.: The rise of graphene. Nature Materials, 6:183, 2007.

20. Wallace, P.: The Band Theory of Graphite. Physical Review, 71:622, 1947.

21. Chen, J.-H., Jang, C., Xiao, S., Ishigami, M., and Fuhrer, M.: Intrinsic and extrinsic performance limits of graphene devices on SiO2. Nature Nanotechnology, 3:206, 2008.

22. X.Hong, Posadas, A., Zou, K., Ahn, C., , and Zhu, J.: High-Mobility Few-Layer Graphene Field Effect Transistors Fabricated on Epitaxial Ferroelectric Gate Oxides. Physical Review Letters, 102:136808, 2009.

23. Peres, N., Neto, A. C., , and Guinea, F.: Conductance quantization in mesoscopic graphene. Physical Review B, 73:195411, 2006.

24. Standley, B., Bao, W., Zhang, H., Bruck, J., Lau, C., , and Bockrath, M.: Graphene-Based Atomic-Scale Switches. Nano letters, 8:3345, 2008.

25. Peres, N., Neto, A. C., and Guinea, F.: Erratum: Conductance quantization in mesoscopic graphene. Physical Review B, 73:239902, 2006.

26. Bourianoff, G., Brillouet, M., Cavin, R., Hiramoto, T., Hutchby, J., Ionescu, A., and Uchida, K.: Nanoelectronics research for beyond CMOS information processing. IEEE Proceedings, 98:1986, 2010.

27. M. Purahmad, M. S. and Dutta, M.: A theoretical study on the effect of piezoelectric charges on the surface potential and surface depletion region of zno nanowires. Semiconductor Science and Technology, 28:015019, 2013.

CITED LITERATURE (Continued)

28. D.L. Robertson, G. J.: Selection in two of an rna enzyme that. specifically cleaves single-stranded dna. Nature, 344:467, 1990.

29. C. Tuerk, L. G.: Systematic evolution of ligands by exponential enrichment: Rna ligands to bacteriophage t4 dna polymerase. Science, 249:505, 1990.

30. A.D. Ellington, J. S.: In vitro selection of rna molecules that bind specific ligands. Nature, 346:818, 1990.

31. O'sullivan, C.: Aptasensorsthe future of biosensing. Anal Bioanal Chem, 372:44, 2002.

32. F. Kleinjung, S. Klussmann, V. E. F. S. J. F. F. B.: Aptamers as specific receptors in bia. Anal Chem, 70:328, 1998.

33. R. Yamamoto, T. Baba, P. K.: Molecular beacon aptamer fluoresces in the presence of tat protein of hiv-1. Genes Cells, 5:389, 2000.

34. X. Fang, A. Sen, M. V. W. T.: Synthetic dna aptamers to detect protein molecular variants in a high-throughput fluorescence quenching assay. ChemBioChem, 4:829, 2003.

35. Xiao, Y., Lubin, A., Heeger, A., and Plaxco, K.: Label-Free Electronic Detection of Thrombin in Blood Serum by Using an Aptamer-Based Sensor. Angewandte Chemie, 117:5592, 2005.

36. R. Lai, K. Plaxco, A. H.: Aptamer-based electrochemical detection of picomolar platelet-derived growth factor directly in blood serum. Anal Chem, 79:229, 2007.

37. A.E. Radi, J.L. Acero Sanchez, E. B. C. O.: Reagentless, reusable, ultrasensitive electrochemical molecular beacon aptasensor. J Am Chem Soc, 44:117, 2006.

38. Xiao, Y., Qu, X., Plaxco, K., and Heeger, A.: Label-Free Electrochemical Detection of DNA in Blood Serum via Target-Induced Resolution of an Electrode-Bound DNA Pseudoknot. Journal of the American Chemical Society, 129:11896, 2007.

39. H.M. So, K. Won, Y. K. B. K. B. R. P. N. H. K. J. L.: Single-walled carbon nanotube biosensors using aptamers as molecular recognition elements. J Am Chem Soc, 127:11906, 2005.

40. Zheng, C., Fan, Z., Wei, T., and Luo, G.: . J. Appl. Polym. Sci., 113:1515, 2009.

CITED LITERATURE (Continued)

41. Bin, L. and Zhong, W.: . J. Mater. Sci., 46:5595, 2011.

42. Stauffer, D. and Aharony, A.: Introduction to Percolation Theory. London, Taylor and Francis, second edition, 1992.

43. Chen, X., Devaux, J., Issi, J., and Billaud, D.: . Polym. Eng. Sci., 35:637, 1995.

44. Straley, J. P.: . Phys. Rev. B., 15:5733, 1977.

45. Nakamura, S., Saita, K., Sawa, G., and Kitagawa, K.: . Jpn. J. Appl. Phys., 36:5163, 1997.

46. Srivastava, N. and Mehra, R.: . J. Appl. Polym. Sci., 109:3991, 2008.

47. Z.Liu, Bai, G., Huang, Y., Feng, D., Li, F., Guo, T., and Chen, Y.: . Carbon, 45:821, 2007.

48. Zheng, W. and Wong, S.: . Compos. Sci. Technol., 63:225, 2003.

49. Ramanathan, T., Stankovich, S., Dikin, D. A., Liu, H., Shen, H., Nguyen, S. T., and Brinson, L. C.: . J. Polym. Sci., 45:2097, 2007.

50. Novoselov, K., Geim, A., Morozov, S., Jiang, D., Zhang, Y., Dubonos, S., Grigorieva, I., and Firsov, A.: . Science, 306:666, 2004.

51. Staley, N., Wang, H., Puls, C., Forster, J., Jackson, T., McCarthy, K., Clouser, B., and Liu, Y.: . Applied Physics Letters, 90:143518, 2007.

52. Xu, K., Erricolo, D., Dutta, M., and Stroscio, M.: . Superlattices and Microstructures, 51:606, 2012.

53. K. Xu, X. Meshik, M. D. and Stroscio, M.: Graphene- and aptamer-based electrochemical biosensor. Nanotechnology, 25:205501, 2014.

54. Bunch, J. S., van der Zande, A. M., Verbridge, S. S., Frank, I. W., Tanenbaum, D. M., Parpia, J. M., Craighead, H. G., and McEuen, P. L.: . Science, 315:490, 2007.

55. Xiao, Y., Qu, X., Plaxco, K., and Heeger, A.: . Journal of the American Chemical Society, 129:11896, 2007.

CITED LITERATURE (Continued)

56. Tuerk, C. and Gold, L.: . Science, 249:505, 1990.

57. Tersoff, J.: . Applied Phyciscs Letters, 74:2122, 1999.

58. Robinson, J. A., LaBella, M., Zhu, M., Hollander, M., Kasarda, R., Hughes, Z., Trumbull, K., Cavalero, R., and Snyder, D.: . Applied Phyciscs Letters, 98:053103, 2011.

59. Bachtold, A., Henny, M., Terrier, C., Strunk, C., C. Schönenberger, J.-P. S., Bonard, J.-M., and Forró, L.: . Science, 249:505, 1990.

60. Wallace, P.: . Physical Review, 71:622, 1947.

61. Campbell, D. J., Higgins, D. A., , and Corn, R. M.: . Journal of Physical Chemistry, 94:3681, 1990.

62. Castro Neto, A., Guinea, F., Peres, N., Novoselov, K., and Geim, A.: . Reviews of Modern Physics, 81:109, 2009.

63. Gilje, S., Han, S., Wang, M., Wang, K., and Kaner, R.: . Nano letters, 7:3394, 2007.

64. Chen, Z., Lin, Y.-M., Rooks, M. J., and Avouris, P.: . Physica E, 40:228, 2007.

65. Tung, V., Allen, M., Yang, Y., , and Kaner, R.: . Nature Nanotechnology, 4:25, 2009.

66. Ohta, T., Bostwick, A., Seyller, T., Horn, K., and Rotenberg, E.: . Science, 313:951, 2006.

67. Kang, Y.-J., Kang, J., , and Chang, K. J.: . Physical Review B, 78:115404, 2008.

68. Baker, B., Lai, R., Wood, M., Doctor, E., Heeger, A., and Plaxco, K.: . Journal of the American Chemical Society, 128:3138, 2006.

69. Chen, R., Zhang, Y., Wang, D., , and Dai, H.: . Journal of the American Chemical Society, 123:3838, 2001.

70. Maehashi, K., Katsura, T., Kerman, K., Takamura, Y., Matsumoto, K., and Tamiya, E.: . Analytical Chemistry, 79:782, 2006.

71. Allen, M., Tung, V., Gomez, L., Xu, Z., Chen, L., Nelson, K., Zhou, C., Kaner, R., , and Yang, Y.: . Advanced Materials, 21:2098, 2009.

CITED LITERATURE (Continued)

72. Moskovits, M.: Surface-enhanced raman spectroscopy: a brief retrospective: a brief retrospective. Journal of Raman Spectroscopy, 36:6, 2005.

73. Merlen, A., Gadenne, V., Romann, J., Chevallier, V., Patrone, L., and Valmalette, J. C.: Surface enhanced Raman spectroscopy of organic molecules deposited on gold sputtered substrates. Nanotechnology, 20:215705, 2009.

74. Vo-Dinh, T.: Surface-Enhanced Raman Spectroscopy Using Metallic Nanostructures. Trends Anal. Chem., 17:557, 1998.

75. P.B.Johnson and Christy, R.: Optical Constants of the Noble Metals. Phys. Rev. B, 6:4370, 1972.

76. Nicolai, S. H. A. and Rubim, J. C.: Surface-Enhanced Resonance Raman (SERR) Spectra of Methylene Blue Adsorbed on a Silver Electrode. Langmuir, 19:4291, 2003.

77. Fan-Ching Chien, Wen Yen Huang, J.-Y. S. C. W. K. and Chen, P.: Revealing the spatial distribution of the site enhancement for the surface enhanced raman scattering on the regular nanoparticle arrays. Optics Express, 17:13974, 2009.

78. S. B. Chaney, S. Shanmukh, R. A. D. and Zhao, Y.-P.: Aligned silver nanorod arrays produce high sensitivity surface-enhanced raman spectroscopy substrates. Applied Physics Letters, 87:3, 2005.

79. Robbie, K., Sit, J. C., and Brett, M. J.: Advanced techniques for glacing angle deposition. J. Vac. Sci. Technol. B, 112:1115, 1998.

80. Yong Yang, Liangming Xiong, J. S. and Nogami, M.: Aligned silver nanorod arrays for surface-enhanced raman scattering. Nanotechnology, 17:2670, 2006.

81. Y.-J. Liu, Z.-Y. Zhang, R. A. D. Y.-P. Z.: The sers response of semiordered ag nanorod arrays fabricated by template oblique angle deposition. Journal of Raman Spectroscopy, 41:1112, 2010.

82. Driskell, J. D., Shanmukh, S., Liu, Y., Chaney, S. B., Tang, X.-J., Zhao, Y.-P., and Dluhy, R.: The Use of Aligned Silver Nanorod Arrays Prepared by Oblique Angle Deposition as Surface Enhanced Raman Scattering Substrates. J. Phys. Chem., 112:895–901, 2008.

CITED LITERATURE (Continued)

83. Xiao, G.-N. and Man, S.-Q.: Surface-enhanced Raman scattering of methylene blue absorbed on cap-shaped silver nanoparticles. Chem. Phys. Lett., 447:305–309, 2007.

84. Otto, C., Van Den Tweel, T. J. J., de Mul, F. F. M., and Greve, J.: Surface-enhanced Raman spectroscopy of DNA bases. J. Raman Spec., 17:289–298, 1986.

85. Vasudev, M., Wu, T.-C., Bitwas, S., Dutta, M., Stroscio, M., Guthrie, S., Reed, M., Burris, K. P., and C. N. Stewart, J.: Optoelectronic Signatures of DNA-Based Hybrid Nanostructures. IEEE Trans. Nanotechnol., 10:35, 2001.

86. Nuntawong, N., Horprathum, M., Eiamchai, P., Wong-ek, K., Patthanasettakul, V., and Chindaudom, P.: Surface-enhanced Raman scattering substrate of silver nanoparticles depositing on AAO template fabricated by magnetron sputtering. Vacuum, 84:1415, 2010.

87. Naujok, R. R., Duevel, R. V., and Corn, R. M.: Fluorescence and Fourier Transform Surface-Enhanced Raman Scattering measurements of Methylene Blue Adsorbed onto a Sulfur-Modified Gold Electrode. Langmuir, 9:1771, 1993.

88. de Araujo Nicolai, S. H., Rodrigues, P. R., Agostinho, S. M., and Rubim, J. C.: Electrochemical and spectroelectrochemical (SERS) studies of the reduction of methylene blue on a silver electrode. Journal of Electroanalytical Chemistry, 527:103, 2002.

89. Niu, Z. and Fang, Y.: Spectrochim. Acta Part A, 66:712, 2007.

90. Stroscio, M. and Dutta, M.: Integrated biological-semiconductor devices. Proceedings of the IEEE, 93:1772, 2005.

91. `http://www.ebioscience.com/knowledge-center/product-line/efluor/efluor-%nanocrystals/imaging.htm`.

92. `http://www.nanoprobes.com/guides/LGuide4.htm`.

93. T. Jennings, M. S. and Strouse, G.: Fluorescent lifetime quenching near d=1.5 nm gold nanoparticles: Probing NSET validity. Journal of the American Chemical Society, 128:5462, 2006.

94. Shu, G. W., Chiu, C. H., Huang, L. T., Lin, T. N., Yang, C. C., Wang, J. S., Yuan, C. T., Shen, J. L., Kuo, H. C., Lin, C. A. J., Chang, W. H., Wang, H. H., Yeh, H. I.,

CITED LITERATURE (Continued)

Chan, W. H., Fan, W. C., and Chou, W. C.: Efficient energy transfer from ingan quantum wells to ag nanoparticles. Phys. Chem. Chem. Phys., 15:3618, 2013.

95. Yun, C. S., Javier, A., Jennings, T., Fisher, M., Hira, S., Peterson, S., Hopkins, B., Reich, N. O., and Strouse, G. F.: Nanometal surface energy transfer in optical rulers, breaking the fret barrier. Journal of the American Chemical Society, 127:3115, 2005.

96. A. Keefe, S. P. and Ellington, A.: Aptamers as therapeutics. Nature Reviews Drug Discovery, 9:537, 2010.

97. Jayasena, S.: Aptamers: An emerging class of molecules that rival antibodies in diagnostics. Clinical Chemistry, 45:1628, 1999.

98. Brenneman, K., Poduri, S., Stroscio, M., and Dutta, M.: Optical Detection of Lead(II) Ions Using DNA-Based Nanosensor. Sensors Journal, IEEE, 13:1783, 2013.

99. Wu, T.-C., Biswas, S., Dutta, M., and Stroscio, M. A.: Quantum-dot-based aptamer beacon for the detection of potassium ions. Nanotechnology, IEEE Transactions on, 10:991, 2011.

100. C. Liu, C. H. and Chang, H.: Highly Selective DNA-Based Sensor for Lead(II) and Mercury(II) Ions. Analytical Chemistry, 81:2383, 2009.

101. Liu, W., Fu, Y., Zheng, B., Cheng, S., Li, W., Lau, T.-C., and Liang, H.: Kinetics and mechanism of conformational changes in a g-quadruplex of thrombin-binding aptamer induced by pb2+. The Journal of Physical Chemistry B, 115:13051, 2011.

102. Rossi, E.: Low level environmental lead exposure–a continuing challenge. Clin Biochem Rev, 29:63, 2008.

103. Surawicz, B., Lepeschkin, E., Herrlich, H. C., and Hoffman, B. F.: Effect of potassium and calcium deficiency on the monophasic action potential, electrocardiogram and contractility of isolated rabbit hearts. Am J Physiol, 196:1302, 1959.

104. Wu, T.-C., Zhao, G., Lu, H., Dutta, M., and Stroscio, M.: Quantum-dot-based aptamer beacons for k detection. Sensors Journal, IEEE, 13:1549, 2013.

CITED LITERATURE (Continued)

105. A. Kratz, M. Ferraro, P. M. S. and Lewandrowski, K. B.: Case records of the massachusetts general hospital. weekly clinicopathological exercises. laboratory reference values. N Engl J Med, 351:1548, 2004.

106. R. White, A. R. and Plaxco, K.: Re-engineering aptamers to support reagentless, self-reporting electrochemical sensors. Analyst, 135:589, 2010.

107. J. Lee, H. So, E. J. H. C. K. W. and Kim, Y.: Aptamers as molecular recognition elements for electrical nanobiosensors. Analytical and Bioanalytical Chemistry, 390:1023, 2008.

108. T. Wu, S. Biswas, M. D. and Stroscio, M.: Quantum-dot-based aptamer beacon for the detection of potassium ions. IEEE Transactions on Nanotechnology, 10:991, 2011.

109. T. C. Wu, G. J. Zhao, H. L. M. D. and Stroscio, M. A.: Quantum-dot-based aptamer beacons for k+ detection. IEEE Sensors Journal, 13:1549, 2013.

110. X. Meshik, K. Xu, M. D. and Stroscio, M.: Optical detection of lead and potassium ions using a quantum-dot-based aptamer nanosensor. IEEE Transactions on NanoBioscience, 13:161, 2014.

111. Maehashi, K. and Matsumoto, K.: Label-free electrical detection using carbon nanotube-based biosensors. Sensors, 9:5368, 2009.

112. T. Chen, T. Phan, C. H. Y. L. J. W.-K. W. C. L. and Li, L.: Label-free detection of dna hybridization using transistors based on cvd grown graphene. Biosensors & Bioelectronics, 41:103, 2013.

113. K. Chen, G. Lu, J. C. S. M. K. Y.-S. C. and Chen, J.: Hg(ii) ion detection using thermally reduced graphene oxide decorated with functionalized gold nanoparticles. Analytical Chemistry, 84:4057, 2012.

114. H. G. Sudibya, Q. He, H. Z. and Chen, P.: Electrical detection of metal ions using field-effect transistors based on micropatterned reduced graphene oxide films. ACS Nano, 5:1990, 2011.

115. A. Keefe, S. P. and Ellington, A.: Aptamers as therapeutics. Nature Reviews Drug Discovery, 9:537, 2010.

CITED LITERATURE (Continued)

116. K. Brenneman, S. Poduri, M. S. and Dutta, M.: Optical detection of lead(ii) ions using dna-based nanosensor. Ieee Sensors Journal, 13:1783, 2013.

117. T. Wu, S. Biswas, M. D. and Stroscio, M.: Quantum-dot-based aptamer beacon for the detection of potassium ions. Ieee Transactions on Nanotechnology, 10:991, 2011.

118. T. C. Wu, G. J. Zhao, H. L. M. D. and Stroscio, M. A.: Quantum-dot-based aptamer beacons for k^+ detection. IEEE Sensors Journal, 13:1549, 2013.

119. C. Liu, C. H. and Chang, H.: Highly selective dna-based sensor for lead(ii) and mercury(ii) ions. Analytical Chemistry, 81:2383, 2009.

120. W. Liu, Y. Fu, B. Z. S. C. W. L.-T. L. and Liang, H.: Kinetics and mechanism of conformational changes in a g-quadruplex of thrombin-binding aptamer induced by pb^{2+}. Journal of Physical Chemistry B, 115:13051, 2011.

121. Y. Xiao, B. D. Piorek, K. W. P. and Heeger, A. J.: A reagentless signal-on architecture for electronic, aptamer-based sensors via target-induced strand displacement. Journal of the American Chemical Society, 127:17990, 2005.

122. B. R. Baker, R. Y. Lai, M. S. W. E. H. D. A. J. H. and Plaxco, K. W.: An electronic, aptamer-based small-molecule sensor for the rapid, label-free detection of cocaine in adulterated samples and biological fluids. Journal of the American Chemical Society, 128:3138, 2006.

123. A. Radi, J. L. A. Snchez, E. B. and O'Sullivan, C. K.: Reagentless, reusable, ultrasensitive electrochemical molecular beacon aptasensor. Journal of the American Chemical Society, 128:117, 2006.

124. Rossi, E.: Low level environmental lead exposure–a continuing challenge. Clin Biochem Rev, 29:63, 2008.

125. A. Kratz, M. Ferraro, P. M. S. and Lewandrowski, K. B.: Case records of the massachusetts general hospital. weekly clinicopathological exercises. laboratory reference values. N Engl J Med, 351:1548, 2004.

126. C. Otto, T. Vandentwell, F. D. and Greve, J.: Surface-ehanced raman-spectroscopy of dna bases. Journal of Raman Spectroscopy, 17:289, 1986.

CITED LITERATURE (Continued)

127. K. Novoselov, A. Geim, S. M. D. J. Y. Z. S. D. I. G. and Firsov, A.: Electric field effect in atomically thin carbon films. Science, 306:666, 2004.

128. I. Meric, M. Han, A. Y. B. O. P. K. and Shepard, K.: Current saturation in zero-bandgap, topgated graphene field-effect transistors. Nature Nanotechnology, 3:654, 2008.

129. Y. Shi, X. Dong, P. C. J. W. and Li, L.: Effective doping of single-layer graphene from underlying sio2 substrates. Physical Review B, 79:115402, 2009.

130. H. Mao, Y. Lu, J. L. S. Z. A. W. and Chen, W.: Manipulating the electronic and chemical properties of graphene via molecular functionalization. Progress in Surface Science, 88:132, 2013.

131. Y. Huang, X. Dong, Y. S. C. L. L. L. and Chen, P.: Nanoelectronic biosensors based on cvd grown graphene. Nanoscale, 2:1485, 2010.

132. J. Robinson, M. LaBella, M. Z. M. H. R. K. Z. H. K. T. R. C. and Snyder, D.: Contacting graphene. Applied Physics Letters, 98:053103, 2011.

133. http://www.horiba.com/us/en/application/material-property-characterization/water-analysis/water-quality-electrochemistry-instrumentation/compact/details/b-731-laquatwin-compact-potassium-ion-meter-17163/.

134. http://www.horiba.com/application/material-property-characterization/water-analysis/water-quality-electrochemistry-instrumentation/electrodes-accessories/ion-electrodes/details/lead-ion-electrode-8008-10c-95%19/.

135. http://www.thermoscientific.com/content/dam/tfs/ATG/EPD/EPD%20Documents/Product%20Manuals%20&%20Specifications/Water%20Analysis%20Instruments%20and%%20Supplies/Lab%20Electrodes%20and%20Sensors/Ion%20Selective%20Electrodes/D1717%2~.pdf.

136. http://www.pasco.com/file_downloads/product_manuals/Lead-Ion-Selective-%Electrode-Manual-CI-6736.pdf.

137. T. Hianik, V. Ostatna, M. S. and Grman, I.: Influence of ionic strength, ph and aptamer configuration for binding affinity to thrombin. Bioelectrochemistry, 70:127, 2007.

CITED LITERATURE (Continued)

138. K. L. Brenneman, B. Sen, M. A. S. and Dutta, M.: Aptamer-based optical bionanosensor for mercury(ii) ions. IEEE Nanotechnology Materials and Devices Conference, page 221, 2010.

139. Stroscio, M. A. and Dutta, M.: Phonons in Nanostructure. Cambridge University Press, 2001.

140. Stojanovic, M., de Prada, P., and Landry, D.: Aptamer-Based Folding Fluorescent Sensor for Cocaine. Journal of the American Chemical Society, 123:4928, 2001.

141. Lai, R., Plaxco, K., and Heeger, A.: Aptamer-Based Electrochemical Detection of Picomolar Platelet-Derived Growth Factor Directly in Blood Serum. Analytical Chemistry, 79:229, 2006.

142. Choi, M. S., Yoon, M., Baeg, J.-O., , and Kim, J.: Label-free dual assay of DNA sequences and potassium ions using an aptamer probe and a molecular light switch complex. Chemical Communications, 47:7419, 2009.

143. Ando, T., Nakanishi, T., , and Saito, R.: Berry's phase and absence of back scattering in carbon nanotubes. Journal of the Physical Society of Japan, 67:2857, 1998.

144. McEuen, P., Bockrath, M., Cobden, D., Yoon, Y.-G., , and Louie, S.: Disorder, Pseudospins, and Backscattering in Carbon Nanotubes. Physical Review Letters, 83:5098, 1999.

145. Paunesku, T., Rajh, T., Wiederrecht, G., Maser, J., Vogt, S., Stojicevic, N., Protic, M., Lai, B., Oryhon, J., Thurnauer, M., and Woloschak, G.: Biology of TiO2Coligonucleotide nanocomposites. Nature Materials, 2:343, 2003.

VITA

NAME	Ke Xu
EDUCATION	Ph.D., Electrical and Computer Engineering, University of Illinois at Chicago, Chicago, Illinois, 2014
	M.S., Electrical and Computer Engineering, University of Illinois at Chicago, Chicago, Illinois, 2013
	B.E., Optical Engineering, Zhejiang University, Zhejiang, China, 2009
EXPERIENCE	Research Assistant, Nanoengineering Research Laboratory, Department of Electrical and Computer Engineering, University of Illinois at Chicago, 08/2010-05/2014
	Teaching Assistant, Department of Electrical and Computer Engineering, University of Illinois at Chicago, 08/2009-12/2013
PUBLICATIONS	K. Xu, M. Purahmed, K. Brenneman, X. Meshik, S. Farid, S. Poduri, P. Pratap, J. Abell, Y. Zhao, B. Nichols, E. Zakar, M. Stroscio, and M. Dutta, "Design and Applications of Nanomaterial-based and Biomolecule-based Nanodevices and Nanosensors" for the "*Design and Applications of Nanomaterials for Devices and Sensors*" within the Springer "*Challenges and Advances in computational Chemistry and Physics*" series; In Press, February 2014.
	K. Xu, X. Meshik, M. Dutta and M. Stroscio, "Graphene- and aptamer-based electrochemical biosensor," *Nanotechnology*, vol. 25, pp. 205501, 2014.
	X. Meshik, K. Xu, M. Dutta and M. Stroscio, "Optical Detection of Lead and Potassium Ions Using a Quantum-Dot-Based Aptamer Nanosensor," *IEEE Transactions on NanoBioscience*, vol. 13, pp. 161, 2014.

VITA (Continued)

K. Xu, P. Pratap, M. Dutta, and M. Stroscio, "Design and Applications of Graphene-based and Biomolecule-based Nanosensors and Nanodevices" for the CRC Press "*Graphene Science Handbook*" Vol. 6 "*Applications and Industrialization*", submitted, July 2013.

K. Xu, J. Qian, and M. Stroscio, Graphene-based Molecule Sensor based on Conformational Change of an Aptamer, *Transaction on Electrical and Electronic Circuits and Systems*, vol. 3, no. 2, 2013

K. Xu, D. Erricolo, M. Dutta and M. Stroscio, "Electrical Conductivity and Dielectric Properties of PMMA/Graphite nanoplatelet ensembles," *Superlattices and Microstructures*, vol. 51, pp. 606-612 (2012).

K. Xu, J. Abell, Y. Zhao, J. Qian, K. Brenneman, X. Meshik, M. Dutta and M. Stroscio, "Surface-Enhanced Raman Spectroscopy as a Tool for Characterization Nanostructure with Molecular Components," *PHONONS*, July 2012, Ann Arbor, Michigan. *AIP Conf. Proc.*, vol. 1506, pp. 57-61 (2012).

K. Xu, J. Qian, P. Shukla, M. Dutta and M. Stroscio, "Graphene-based FET Structure: Modeling FET Characteristics for an Aptamer-based Analyte Sensor," *IEEE Conf. Proc.* of 15th International Workshop on Computational Electronics, May 2012.

X. Meshik, K. Brenneman, K. Xu, J. Abell, Y. Zhao, M. Dutta, M. Stroscio, "Surface-Enhanced Raman Spectroscopy Signatures of an RNA Molecule: An Aptamer that Binds to the $\alpha V\beta 3$ Integrin", *PHONONS* 2012, July 8-12, 2012, Ann Arbor, Michigan. *AIP Conf. Proc.* 1506, pp. 49-52 (2012).

K. L. Brenneman, X. Meshik, K. Xu, J. Abell, Y. Zhao, M. Dutta, and M. A. Stroscio, "Surface-Enhanced Raman Spectroscopy Study of Single Stranded DNA Sequences on Silver Nanorod Array" *PHONONS* 2012, July 8-12, 2012, Ann Arbor, Michigan. *AIP Conf. Proc.* 1506, pp. 53-56 (2012).

M. Dutta, M. Stroscio, J. Qian, T. Wu, K. Brenneman, B. Sen, K. Xu, S. Poduri, X. Meshik, S. Ranginwala, P. Shukla and N. Zhang, "Nanosensors Based on DNA and RNA Aptamers and Semiconductor Quantum Dots," *CRC Dekker Encyclopedia of Nanoscience and Nanotechnology*,

VITA (Continued)

Jun 2012.

PRESENTATIONS

K. Xu, J. Qian, M. A. Stroscio, and M. Dutta, "Graphene Surface as Aptamer Binding Site for a Graphene-based FET Structure", *American Vacuum Society Priairie Chapter Symposium*, Evanston, IL, 2011.

M. Stroscio, M. Dutta, B. Sen, K. Xu, J. Qian, and K. Sun, "Phonons in Nanostructures", *Phonon School, International Workshop on Computational Electronics*, University of Wisconsin, Madison, WI, June 2012. (Invited)

K. Xu, J. Qian, P. Shukla, M. Dutta and M. Stroscio, "Graphene-based FET Structure: Modeling FET Characteristics for an Aptamer-based Analyte Sensor," *15th International Workshop on Computational Electronics*, Madison, WI, May 2012.

K. Xu, J. Abell, Y. Zhao, J. Qian, K. Brenneman, X. Meshik, M. Dutta and M. Stroscio, "Surface-Enhanced Raman Spectroscopy as a Tool for Characterization Nanostructure with Molecular Components," *XIV International Conference on Phonon Scattering in Condensed Matter (Phonons 2012)* July 2012, Ann Arbor, Michigan.